The Astrophysical Journal, 896:49 (17pp), 2020 June 10 https://doi.org/10.3847/1538-4357/ab85cd

Three Lyα Emitting Galaxies within a Quasar Proximity Zone at $z \sim 5.8$

Sarah E. I. Bosman[1], Koki Kakiichi[1,2], Romain A. Meyer[1], Max Gronke[2], Nicolas Laporte[3,4], and Richard S. Ellis[1]
[1] Department of Physics and Astronomy, University College London, London, UK; s.bosman@ucl.ac.uk
[2] Department of Physics and Astronomy, University of California, Santa Barbara, CA, USA
[3] Kavli Institute for Cosmology, University of Cambridge, Cambridge, UK
[4] Cavendish Laboratory, University of Cambridge, Cambridge, UK
Received 2019 December 24; revised 2020 March 19; accepted 2020 March 30; published 2020 June 11

Abstract

Quasar proximity zones at $z > 5.5$ correspond to overdense and overionized environments. Galaxies found inside proximity zones can therefore display features that would otherwise be masked by absorption in the intergalactic medium. We demonstrate the utility of this quasar-galaxy synergy by reporting the discovery of the first three "proximate Lyα emitters" (LAEs) within the proximity zone of quasar J0836+0054 at $z = 5.795$ (Aerith A, B, and C). Aerith A, located behind the quasar with an impact parameter $D_\perp = 278 \pm 8$ pkpc, provides the first detection of an Lyα transverse proximity effect. We model the transmission and show that it constrains the onset of J0836's quasar phase to 0.2Myr $< t <$ 28Myr in the past. The second object, Aerith B at a distance $D < 912$ pkpc from the quasar, displays a bright and broad double-peaked Lyα emission line. The peak separation implies a low ionizing $f_{\rm esc} \lesssim 1\%$. We fit the Lyα line with an outflowing shell model, finding a typical central density $\log N_{\rm H\,I}/{\rm cm}^{-2} = 19.3^{+0.8}_{-0.2}$, outflow velocity $v_{\rm out} = 16^{+4}_{-11}$ km s^{-1}, and gas temperature $\log T/K = 3.8^{+0.8}_{-0.7}$ compared to $2 < z < 3$ analog LAEs. We detect object Aerith C via an Lyα emission line at $z = 5.726$. This corresponds with the edge of the quasar's proximity zone ($\Delta z < 0.02$), suggesting that the proximity zone is truncated by a density fluctuation. Via the analyses conducted here, we illustrate how proximate LAEs offer unique insight into the ionizing properties of both quasars and galaxies during hydrogen reionization.

Unified Astronomy Thesaurus concepts: Lyman-break galaxies (979); Lyman alpha forest (980); Spectroscopy (1558); Quasar-galaxy pairs (1316); Quasars (1319); Galaxies (573); Galaxy formation (595); Reionization (1383); Early universe (435)

Supporting material: animation

1. Introduction

Reionization, the phase transition that rendered intergalactic hydrogen-ionized, is thought to have concluded by $z \sim 5.5$ (Fan et al. 2006; Greig et al. 2017). Mysteries regarding the morphology and driving sources of the process persist across a range of scales.

The unfolding of reionization during its end stages at $z \leqslant 6.0$ has been tracked in great detail using Lyα transmission along the lines of sight to bright quasars (Fan et al. 2006; McGreer et al. 2015; Bosman et al. 2018; Eilers et al. 2018). Correlations in intergalactic medium (IGM) Lyα opacity across $\gtrsim$40 proper Mpc (pMpc) have ruled out a homogeneous UV background (UVB) during the late stages of reionization (Becker et al. 2015b, 2018; Kashino et al. 2020), requiring the addition of mean free path and temperature fluctuations, an evolution of the global galaxy ionizing emissivity, and/or an increased contribution from rare ionizing sources (Chardin et al. 2015; Davies & Furlanetto 2016; Keating et al. 2016; Kulkarni et al. 2019).

On small scales, faint galaxies with UV magnitude $M_{\rm UV} > -18$ are expected to be the primary drivers of reionization (Robertson et al. 2013; Dijkstra et al. 2016; Stark 2016). The number of ionizing photons provided by a galaxy is the product of its ionizing emissivity, $\xi_{\rm ion}$, and the escape fraction of these photons from the galaxy, $f_{\rm esc}$. For galaxies with the same $M_{\rm UV}$, models indicate that at least one of these parameters needs to be larger at $z > 5.8$ than at $z \lesssim 3$ in order for faint galaxies to provide the totality of the reionization photon budget (Robertson et al. 2015; Kakiichi et al. 2018; Meyer et al. 2019b, 2019c). However, the identification and study of early galaxies is complicated by the opacity of the IGM to wavelengths $\lambda < 1215$ Å. Direct detection of Lyman-continuum (LyC) emission is currently only possible in the highly ionized IGM at $z \lesssim 4$ (e.g., Prochaska et al. 2009; Worseck et al. 2014; Fletcher et al. 2019).

Neutral hydrogen also hinders the use of the Lyα emission line at $z > 5$, the most common feature observed in the optical. The number of continuum-selected Lyman-break galaxies (LBGs) that display Lyα emission drops beyond $z > 6$ (Ouchi et al. 2010), most likely due to extended absorption wings in extremely neutral environments (Dijkstra et al. 2007; Laursen et al. 2011; Mesinger et al. 2015; Weinberger et al. 2018). Luminous galaxies are less affected by the decline in Lyα visibility (Santos et al. 2016; Zheng et al. 2017; Konno et al. 2018; Mason et al. 2018) owing to their probable location within early ionized bubbles that facilitates their observation (Matthee et al. 2015; Songaila et al. 2018). In addition, the observed shape of the Lyα line is also affected by reionization. At $z < 4$, the Lyα emission line occasionally displays a double-peaked shape whose morphology correlates with the presence of LyC leakage (Verhamme et al. 2015; Izotov et al. 2018; Vanzella et al. 2018) as well as a wide range of galactic properties (Gronke 2017; Marchi et al. 2018). At $z > 5$, the visibility of the blue peak of the Lyα emission line is strongly suppressed (Matthee et al. 2017; Shibuya et al. 2018), limiting its usefulness.

Currently, the only $z > 5$ double-peaked Lyα emitters (LAEs) are NEPLA4 at $z = 6.55$ (Songaila et al. 2018; Mason et al. 2018) and COLA1 at $z = 6.59$ (Hu et al. 2016). Modeling of the Lyα double peak in COLA1 and comparison with lower-z analogs have yielded highly detailed information, including

estimates of its interstellar medium (ISM) temperature $T \sim 16,000$ K, a relatively low central neutral hydrogen density $N_{\rm H\,I} \sim 10^{17}$ cm^{-2}, as well as dust opacity, velocity dispersion, and outflow speed (Matthee et al. 2018). Further, the small velocity separations between the blue and red peaks of Lyα in both COLA1 and NEPLA4 (220 km s^{-1} and 300 km s^{-1}, respectively) indicate an elevated $f_{\rm esc} \gtrsim 0.1$ (Izotov et al. 2018), suggesting these objects could be contributing to their own locally ionized environments. While such insight into reionization-era galaxies is invaluable, both of these galaxies are among the brightest at $z > 6.5$ and display Lyα luminosities $\sim$7 times higher than those found in LAEs at $z \sim 3$ and related analogs such as Green Pea (GP) galaxies (e.g., Yamada et al. 2012; Yang et al. 2017). While they are tracing exceptionally highly ionized regions during the epoch of reionization (EoR), COLA1 and NEPLA4 may not be representative of the faint galaxies responsible for the bulk of the process.

Quasar proximity zones offer an alternative way of tracing over-ionized regions during reionization. Even in the significantly neutral IGM at $z > 5.5$, luminous quasars are observed to be surrounded by ionized H II regions sustained by the ionizing radiation from the active galactic nucleus (AGN; e.g., Madau & Rees 2000; Wyithe et al. 2005; Bolton et al. 2011). In addition, UV-selected bright quasars ($M_{\rm AB} < -27$) at $5.5 < z < 6.0$ reside in highly star-forming host galaxies (Walter et al. 2009) with large reservoirs of molecular gas (Decarli et al. 2018 and therein) and are expected to be hosted in dark matter haloes of masses $M_h \gtrsim 10^{12}$ (Shen et al. 2007; Conroy & White 2013). As such, the locations of EoR quasars should coincide with the most active sites of early galaxy formation (e.g., Overzier et al. 2009). Proximity zones are ideal locations to observe reionization-era galaxies:

1. they correspond to over-dense environments; and
2. the quasar clears the neutral hydrogen responsible for the attenuation of the Lyα emission of galaxies, revealing features normally masked by IGM absorption.

In this paper, we demonstrate the power of galaxies found in quasar proximity zones, or proximate LAEs, to constrain the ionizing properties of EoR galaxies and quasars. We present the first three proximate LAEs: hereafter, Aerith A, B, and C. All three are observed to have unique properties linked to their location.

The observational data and derived physical properties of the objects are given in Section 2. In Section 3, we explore the morphology of the double-peaked LAE Aerith B and model the Lyα emission line using an expanding shell model. Section 4 discusses the structure of J0836's proximity zone inferred from a diagonally transverse proximity effect detected toward Aerith A. Modeling the transmission yields limits on the timescale of the quasar's activity. We discuss implications for reionization in Section 5 and summarize in Section 6.

Throughout the paper, we use a flat ΛCDM cosmology with $\Omega_m = 0.3089$ and $H_0 = 67.74$ (Planck Collaboration et al. 2016). Magnitudes are given in the AB system (Oke & Gunn 1983) and distances are quoted in proper distance units unless otherwise specified. We use F and $\overline{F}$ to distinguish between measurements of flux and flux density (per Å), respectively. Observational sensitivity uncertainties are denoted with (sys) while calibration uncertainties are indicated with (obs). At $z = 5.8$, $1' \simeq 0.24$ pMpc and a redshift interval $\Delta z = 0.05 \simeq 3.4$ pMpc.

2. Observations

SDSS J0836+0054 (J0836) is the third brightest quasar currently known at $z > 5.7$ out of more than 313 objects (Fan et al. 2001; Bañados et al. 2016; Bosman 2020). It is also one of the most radio-loud quasars at $z > 5.7$ out of $\sim$50 for which data is available (Wang et al. 2007; Bañados et al. 2015, 2018a). In this paper, we make use of a 2.3 hr Very Large Telescope/X-Shooter spectrum (Vernet et al. 2011) originally presented in McGreer et al. (2015) and re-reduced in Bosman et al. (2018). Estimates of J0836's systemic redshift have varied widely in the literature (e.g., Stern et al. 2003: $z = 5.774 \pm 0.003$; Shen et al. 2019: $z = 5.834 \pm 0.007$) due to the variety of methods used in the absence of detected molecular lines from the host galaxy (Maiolino et al. 2007). Among optical and infrared emission lines, Mg II 2800 Å is most often used to estimate the systemic redshift due to its relative agreement with host [C II] 158 μm emission (e.g., Decarli et al. 2018). Unfortunately, Mg II is heavily affected by atmospheric water absorption in our X-Shooter spectrum of J0836, as well as in an older ISAAC spectrum (Kurk et al. 2007). More than 50% of the Mg II line flux is lost to telluric absorption in both spectra, making measurements of the black hole mass, redshift, and Eddington ratio tenuous. Instead, we use a combination of the O I 1305 Å and C II 1335 Å emission lines as a proxy for Mg II. We determine the wavelengths of peak emission of the two lines using the QUICFit algorithm.[5] This yields a redshift of $z_{\rm O\,I+C\,II} = 5.804 \pm 0.002$(measurement uncertainty). To evaluate the bias and uncertainty of this estimate, we use the 23 quasars at $z > 5.4$ from Meyer et al. (2019a). On average, O I and C II display small shifts and scatter from the Mg II emission line of $\Delta v_{\rm (O\,I + C\,II) - Mg\,II} = -48 \pm 136$ km s^{-1} when the two lines are treated as independent measurements. In addition, the Mg II emission line has been shown to display a systematic blueshift compared to [C II] at $z \gtrsim 6$ (Venemans et al. 2016; Mazzucchelli et al. 2017). We use the value of $\Delta v_{\rm Mg\,II - [C\,II]} = -350 \pm 500$ km s^{-1} from an upcoming compilation by J.-T. Schindler et al. (2020, in preparation). Taking both of these biases and uncertainties into account yields a redshift of $z_{\rm sys} = 5.795 \pm 0.012$, which we will use throughout the paper.

In order to estimate the transmitted Lyα flux inside J0836's proximity zone, we fit a physically motivated emission model to its continuum and the Lyα, N V 1240 Å, and Si II 1260 Å emission lines. A power law is fitted to the continuum over wavelength intervals devoid of emission lines (Bosman et al. 2018). We use four Gaussian components to represent the broad and narrow components of Lyα emission and the single-component N V and Si II lines. The emission line components are permitted to have a (single) velocity shift with respect to the quasar systemic redshift, which we find to be $\Delta v = 150 \pm 30$ km s^{-1}. More sophisticated methods for reconstructing the shape of the Lyα emission complex (e.g., Greig et al. 2017; Eilers et al. 2018; Davies et al. 2019; Durovčíková et al. 2020) may predict slightly different strengths of intrinsic emission.

2.1. SuprimeCam Photometry

Observations with SuprimeCam on the 8.2 m Subaru Telescope (Kaifu et al. 2000; Miyazaki et al. 2002) were conducted in a $34' \times 27'$ field of view around J0836 in 2004 (Ajiki et al. 2006; P.I. Taniguchi). The field was imaged with

[5] https://github.com/rameyer/QUICFit

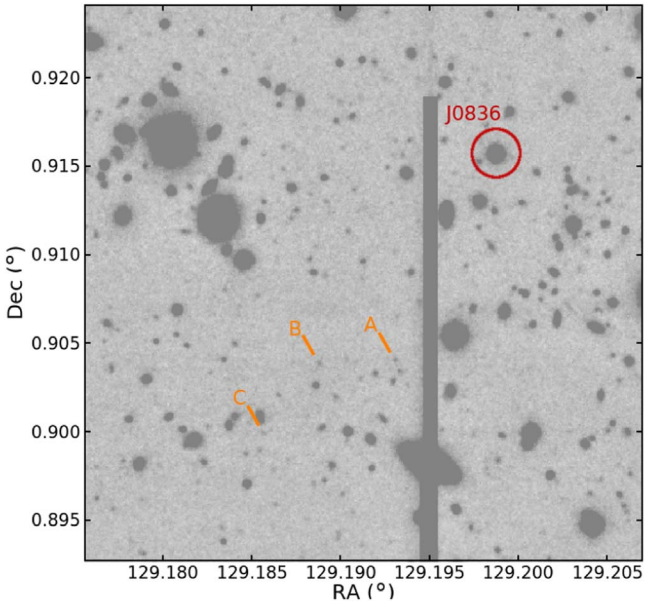

Figure 1. Layout of the field around quasar J0836. The z broadband image is shown, with contamination from a nearby star masked by a vertical rectangle.

the *B, V, r+, i+, z+* (hereafter *r, i, z*) broadband filters as well as the narrowband filter NB816 corresponding to Lyα over $5.65 < z_{\mathrm{Ly}\alpha} < 5.75$ (50% transmission bounds). The seeing in individual exposures was $<1\farcs2$ at all times. In another study, we aimed to identify LBGs around J0836 at $5.65 \leqslant z \leqslant 5.90$ (Meyer et al. 2019c). We initially selected candidates for spectroscopic follow up based on their *r*, *i*, and *z* magnitudes. Our selection criteria are described in Kakiichi et al. (2018) and Meyer et al. (2019c) and briefly summarized here. We search an area of $\sim 10'$ radius around the quasar for objects with $(r-i) > 1.0$ and $(i-z) < 1.0$ colors and a 3σ detection in the z band. We then prioritize for follow up of the objects with $(r-i) > 1.5$ and no detections in the *r* band, and finally, we use filler objects with narrow photometric redshift posteriors regardless of $(i-z)$ color. Zheng et al. (2006, hereafter Z06) used Hubble Space Telescope (HST)/Advanced Camera for Surveys (ACS) photometry and slightly different selection criteria to identify seven ($i_{\mathrm{ACS}} - z_{\mathrm{ACS}}$) dropouts in the central $3'$ radius around J0836; we identify 19 candidates over the same area out of which three overlap with their selection (objects "A", "B", and "F" in their paper). Of these 19 candidates, we spectroscopically followed up 11, including Z06's "A" and "B" (Section 2.2). Three of these (dubbed Aerith A, B, and C,) that lie in the proximity zone form the basis of this paper. Their location with respect to J0836 is shown in Figure 1.

Noting the importance of these three sources, we decided to carefully re-reduce the SuprimeCam archival observations to attain more accurate photometry in the *i* and *z* bands and obtain measurements in the NB816 filter. The re-reduction was carried out using the legacy pipeline `SDFRED1` (Yagi et al. 2002; Ouchi et al. 2004). Magnitudes are extracted using `SExtractor` (Bertin & Arnouts 1996), and the limiting magnitude is estimated by distributing forced apertures in the $1' \times 1'$ region surrounding the central quasar. We noticed infrared fringing around bright objects in the z band that might have been affecting the initial photometry of Aerith A, as well as a lower effective seeing in this band of $\sim 2''$. We therefore conservatively extract the total fluxes in $3''$ apertures, which do not contain any visible contaminating objects for our targets of interest (Figure 2). Additionally, we mitigate the effect of fringing by masking the affected regions. This reduces the depth of the z-band photometry by 14% at the location of Aerith A. Zero-pointing of the photometry was carried out using 14 faint quasars and stars within the field of view with spectra available in the Sloan Digital Sky Survey Data Release 4 (SDSS DR4; Blanton et al. 2017). We find this to be the dominant source of flux uncertainties, due to the nonlinearity of the zero-point correction with magnitude and the relative lack of sufficiently faint standard sources. The measured scatter is of the order of 25% at 2σ in all bands. Our measured sensitivities (Table 1) are $\lesssim 1.5\sigma$ worse than those reported by Ajiki et al. (2006, hereafter A06), who first presented the SuprimeCam observations, when accounting for the smaller $1''$ apertures used by those authors. Using a $1''$ aperture, we obtain flux measurements consistent at 1σ with A06 for Aerith A and Aerith C (A06's "A" and "B", respectively; Table 2) in all bands, except for z(Aerith A) where we obtain $\overline{F_z} = 9.04 \times 10^{-20}$ erg s^{-1} cm^{-2} Å^{-1}, in closer agreement with Z06's HST/ACS values.

2.2. DEIMOS Spectroscopy

Spectroscopic follow up was conducted with the DEep Imaging Multi-Object Spectrograph (DEIMOS; Faber et al. 2003) on the 10 m Keck II telescope on 2018 March 7 and 8, with the primary goal of confirming $5.65 \leqslant z \leqslant 5.90$ LBGs candidates to use for cross-correlation with the Lyα transmission toward J0836 (Meyer et al. 2019c). The total exposure time was 19,000 s (5.27 hr) with an average airmass of 1.099 (P.I.D. U182, P.I. Robertson). The DEIMOS field of view covers a slit mask area of $16\farcm7 \times 5'$ so that the central $5' \times 5'$ area is entirely covered. Due to constraints in mask design, candidates were followed up to maximize efficiency and their likelihood of being $5.65 < z < 5.90$ LBGs, also referred to as their grade. We observed 32 targets in J0836's field. We used a $1''$ slit with the 600ZD grating providing coverage over $4950 < \lambda(\text{Å}) < 10,000$ at a spectral resolution of 3.5 Å. Full details of our DEIMOS observations are given in Meyer et al. (2019c).

The data were reduced with the DEIMOS DEEP2 Data Reduction Pipeline (Cooper et al. 2012; Newman et al. 2013) as well as with the open-source code *Pypeit* (Prochaska et al. 2019) to check for consistency. In both cases, the reduction was performed in the standard way using the same standard star and taking slit losses into account. While extracted fluxes from the two reductions agree within 1σ, the DEEP2 reductions achieved signal-to-noise ratios (S/N) 8% larger on average, and we use them in the rest of the paper. We suspect this to be caused by subtle differences in the slit-tracing and co-addition algorithms involved in the reduction pipelines, and we note that *Pypeit* is currently in a pre-release state with improvements being made frequently.

The search for the lines was conducted visually by five of the authors (S.E.I.B., R.M., R.S.E., N.L., and K.K.) while being blind to individual targets' grades, photometric redshifts, and y-positions across the slit (which were scrambled to maximize mask efficiency). We identified four emission lines that were revealed to lie at the y-position of the targeted dropouts. A confirmed LAE at $z = 5.284$, at a distance $d = 39$ pMpc from the quasar line of sight, is used in the analysis of Meyer et al. (2019c).

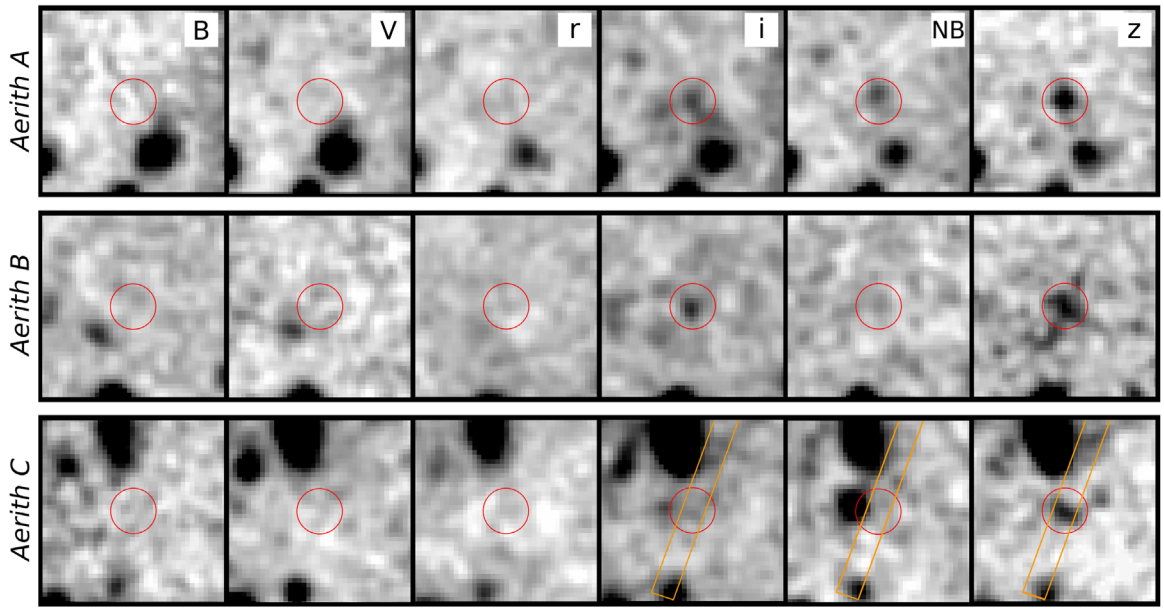

Figure 2. Subaru/SuprimeCam photometry of the proximate LAEs. The narrowband filter NB816 corresponds to $5.65 < z_{\mathrm{Ly}\alpha} < 5.75$. A 10σ detection of Aerith A can be seen in NB816, corresponding to emission bluewards of its $z_{\mathrm{sys}} = 5.849 \pm 0.004$. Aerith C shows a physical offset between the peak emission in the z band and the NB816 and i bands of 6.3 pkpc assuming $z_{\mathrm{sys}} = 5.722$. The red circles are $3''$ in radius, and the DEIMOS slit position is shown in orange for Aerith C.

Table 1
Photometry of the $34' \times 27'$ Field around J0836 with Subaru-SuprimeCam

	B	V	r	i	z	$NB816$
t_{exp} (s)	6000	14400	3600	5920	9630	10800
depth (3σ)	28.2	28.4	27.9	27.6	26.4	27.2

Note. Magnitudes are calculated within a $2''$ aperture except for the z broad band, which uses a $3''$ aperture.

2.3. Individual Objects

2.3.1. Aerith A

At the location of Aerith A, we detect an emission line at $\lambda = 8334.7$ Å with S/N > 20 (Figure 3). No other emission lines are visible in the range $5000 < \lambda < 9550$ Å. A faint continuum is detected at 5.3σ redwards of the emission line, with intensity $\overline{F}_{\mathrm{cont,spec}} = 8.5 \pm 1.6(\mathrm{obs}) \pm 0.6(\mathrm{sys}) \times 10^{-20}$ erg s^{-1} cm^{-2} Å^{-1}over $9050 < \lambda < 9305$ Å. This is in agreement with the photometry in the z band. No continuum is visible bluewards of the emission line. Taken together with the absence of other emission lines, this step in the continuum unambiguously identifies this object as an LBG and the emission line as Lyα. We fit the line with a Gaussian, obtaining a best-fit line redshift of $z_{\mathrm{Ly}\alpha} = 5.856 \pm 0.003$ and an equivalent width $\mathrm{EW}_{\mathrm{Ly}\alpha} = 18 \pm 4$ Å. The Lyα line shows systematic velocity offsets from nebular lines that anticorrelate with its EW (Erb et al. 2014; Cassata et al. 2020). Based on the sample of Erb et al. (2014), we estimate the velocity offset to be $\Delta v = 295 \pm 138$ km s^{-1} in Aerith A, implying a systemic $z_{\mathrm{sys}} = 5.849 \pm 0.004$. This corresponds to a distance $D_{\parallel} = 3.52$ pMpc behind the quasar.

The object is also detected at 10σ in the NB816 filter (Figure 2, top panel). We stack the DEIMOS spectrum multiplied by the narrowband transmission curve and obtain a corresponding measurement limit of $\overline{F}_{\mathrm{NB,\ spec}} < 4.4 \times 10^{-20}$ erg s^{-1} cm^{-2} Å^{-1}at 2σ .

The 90% transmission range of the NB816 filter is $8056 < \lambda < 8239$ Å, corresponding to shorter wavelengths than the Lyα emission line of Aerith A: this object possesses a faint blue continuum. The window of transmission extends from 1.7 to 11.8 pMpc in front of the quasar such that ⩾34% of the width of the narrow band lies within the quasar's proximity zone. We conclude that this transmission is likely the result of significantly ionized foreground hydrogen: the quasar's proximity zone detected *transversely* by a background LBG. Under this interpretation, we calculate an integrated transmission $T = \overline{F}_{\mathrm{NB}}/k\overline{F}_z = 37 \pm 6(\mathrm{sys})^{+22}_{-13}(\mathrm{sys})\%$, where $k(\beta)$ is a continuum scaling factor depending on the spectral slope.[6] The non-detection of the continuum in the DEIMOS spectrum yields $T < 39\%$ at 2σ, for a combined constraint of $T = 30 \pm 11\%$. We therefore measure an Lyα opacity over the narrow band $\tau_{\mathrm{NB}} = -\ln(T) = 1.2^{+0.4}_{-0.3}$.

2.3.2. Aerith B

Aerith B displays two emission lines at $\lambda\lambda = 8251$, 8267 Å with a velocity separation of $\Delta v_{\mathrm{sep}} = 580 \pm 80$ km s^{-1} (Figure 4). The separation is incompatible with an [O II] 3727, 3730 Å doublet at $z = 0.2282$ ($\Delta v_{\mathrm{sep}} = 224$ km s^{-1}), the only common emission line doublet with $\Delta v_{\mathrm{sep}} < 1000$ km s^{-1}. We measure the ratio of fluxes $A = F_{\mathrm{blue}}/F_{\mathrm{red}} = 0.65 \pm 0.05$. While some extreme [O II] emitters do display similarly skewed emission ratios, none show such wide velocity separations (Paulino-Afonso et al. 2018). We conclude that Aerith B is a double-peak Lyα emitter at $z_{\mathrm{Ly}\alpha} \simeq 5.793$ (see Section 3.4 for further fitting and modeling). Using the detection in the z band to estimate the continuum, we measure the equivalent width of the two Lyα emission components on either side of the trough at $\lambda = 8260$ Å (Figure 4) as $W_{\mathrm{red}} = 36^{+17}_{-11}$ Å; $W_{\mathrm{blue}} = 23^{+11}_{-7}$ Å.

[6] For $\beta = -2$ as we assume throughout, $k = 1.25$. For reference, $k = 1.12$ for a slope $\beta = -1$.

Table 2
Summary of Important Measurements and Inferred Quantities

	Aerith A	Aerith B	Aerith C
α_{J2000}	08:36:45.24	08:36:46.28	08:36:47.04
δ_{J2000}	00:54:11.20	00:54:10.55	00:53:56.36
F_i (10^{-17} erg s^{-1} cm^{-2})	$7.8^{+2.9}_{-1.7}$	$4.9^{+1.9}_{-1.1}$	$3.9^{+1.4}_{-0.8}$ [a]
$\overline{F_z}$ (10^{-20} erg s^{-1} cm^{-2} Å^{-1})	$9.0 \pm 0.8(\mathrm{obs})^{+2.0}_{-1.3}(\mathrm{sys})$	$7.4 \pm 0.9(\mathrm{obs})^{+1.7}_{-1.0}(\mathrm{sys})$	$6.2 \pm 0.5(\mathrm{obs})^{+1.3}_{-0.9}(\mathrm{sys})$
F_{NB816} (10^{-18} erg s^{-1} cm^{-2})	$5.0 \pm 0.4(\mathrm{obs})^{+2.0}_{-1.1}(\mathrm{sys})$	<2.3	$23.0 \pm 1.0(\mathrm{obs})^{+9.0}_{-5.0}(\mathrm{sys})$
$F_{\mathrm{Ly}\alpha,\mathrm{spec}}$ (10^{-18} erg s^{-1} cm^{-2})	$10.9 \pm 0.5(\mathrm{obs})^{+0.7}_{-0.6}(\mathrm{sys})$	$30.1 \pm 0.5(\mathrm{obs})^{+1.8}_{-1.6}(\mathrm{sys})$	$2.1 \pm 0.3(\mathrm{obs})^{+0.3}_{-0.2}(\mathrm{sys})$
$z_{\mathrm{Ly}\alpha,\mathrm{peak}}$	5.856 ± 0.003	5.799 ± 0.003	5.726 ± 0.003
z_{sys}	5.849 ± 0.004	5.7941 ± 0.0003	5.722 ± 0.004
$D_\perp$ (pkpc)	278 ± 8	334 ± 8	446 ± 8
D_{QSO} (pkpc)	3520 ± 820	339^{+573}_{-5}	4920 ± 790
$\mathrm{EW}_{\mathrm{Ly}\alpha,\mathrm{phot}}$ (Å,rest)	>10.1	76^{+55}_{-34}	55^{+8}_{-5}
$\mathrm{EW}_{\mathrm{Ly}\alpha,\mathrm{spec}}$ (Å,rest)	18 ± 4	59^{+28}_{-18}	$5.0^{+1.4}_{-0.5}$
M_{UV}	-21.3 ± 0.2	$-21.0^{+0.3}_{-0.2}$	-20.8 ± 0.2
$\log L_{\mathrm{Ly}\alpha}$ (erg s^{-1})	$42.63^{+0.05}_{-0.04}$	43.03 ± 0.03	$42.93^{+0.15}_{-0.11}$ [a]
$\mathrm{SFR}_{\mathrm{UV}}(M_\odot\ \mathrm{yr}^{-1})$	24^{+5}_{-4}	19^{+5}_{-2}	16^{+4}_{-2}
$\mathrm{SFR}_{\mathrm{Ly}\alpha}(M_\odot\ \mathrm{yr}^{-1})$	49^{+22}_{-13}	38^{+21}_{-14}	32^{+18}_{-10} [a]

Notes. Photometric rest-frame equivalent widths assume a flat spectral slope $\beta = -2$ and $z_{\mathrm{Ly}\alpha}$. Inferred values for Aerith C assume that the z band and NB816 detection are physically related. Limits are given at the 2σ level.
[a] Based on photometry.

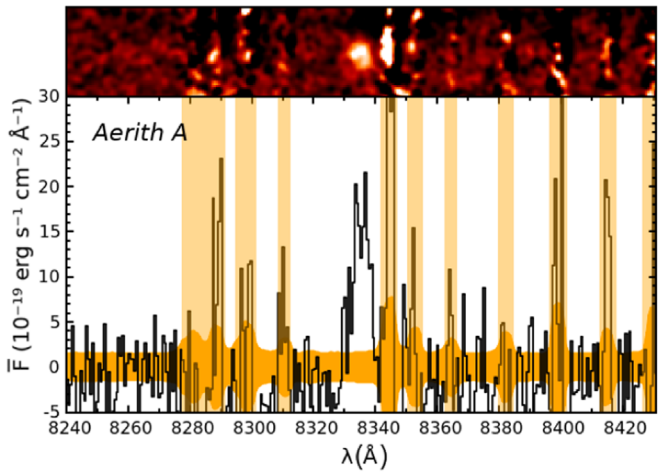

Figure 3. DEIMOS spectroscopy of Aerith A. The lack of detection of the other lines and a step in the continuum emission identify this as an Lyα emission line at $z_{\mathrm{Ly}\alpha} = 5.856$ (Section 2.3.1). In this figure and all that follow, sky-lines are masked by vertical orange rectangles.

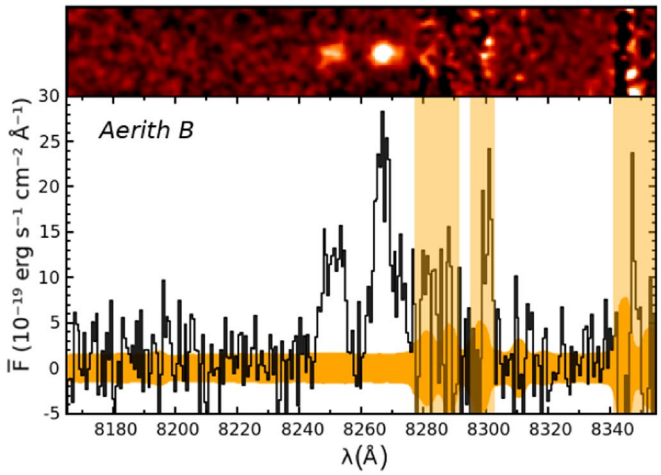

Figure 4. DEIMOS spectroscopy of the two emission lines in Aerith B. The velocity separation between the peaks (580 ± 80 km s^{-1}) is incompatible with any common emission line doublets from a low-z interloper. The double-peaked morphology is typical among double-peaked LAEs at $2 < z < 3$.

Stacking the extracted spectrum over $9050 < \lambda < 9305$ Å as for Aerith A reveals a 4.6σ detection of $\overline{F}_{\mathrm{cont,spec}} = 6.5 \pm 1.4(\mathrm{obs}) \pm 0.5(\mathrm{sys}) \times 10^{-20}$ erg s^{-1} cm^{-2} Å^{-1}, in agreement with the z-band photometric detection. The object is not detected in NB816 at 2σ either photometrically or spectroscopically. We combine the two constraints into a loose upper limit $\overline{F}_{\mathrm{NB}} < 3.1 \times 10^{-20}$ erg s^{-1} cm^{-2} Å^{-1} at 2σ. The resulting fractional transmission over the narrow band is $T = \overline{F}_{\mathrm{NB}}/k\overline{F}_z <$ 34% at 2σ, or $\tau_{\mathrm{NB}} > 1.1$.

2.3.3. Aerith C

We detect an emission line at $\sim 7\sigma$ above the noise at $\lambda =$ 8176.9 Å in Aerith C (Figure 5). Stacking the redward continuum yields a 2σ upper limit $\overline{F}_{\mathrm{cont,spec}} < 5.2$ erg s^{-1} cm^{-2} Å^{-1}. This is in 2σ tension with the higher value from photometry. No other lines are detected in this spectrum, but the relative weakness of the line makes ruling out an interloping object more challenging. Complementary evidence is provided by the NB816 image (Figure 2, bottom panel). The NB816 wavelength range ideally encompasses the detected emission line. However, there is a large physical offset between the peaks of the z-band and NB816 emission, corresponding to 6.27 pkpc at $z_{\mathrm{Ly}\alpha} = 5.726$. The positioning of the DEIMOS slit (orange rectangle, Figure 2) was unfortunate in that the z-band continuum was centered while missing most of the NB816 emission. Indeed, the photometry indicates a much larger flux in the NB816 than we observed spectroscopically (Table 2): only ∼9% of the emission line flux was recorded

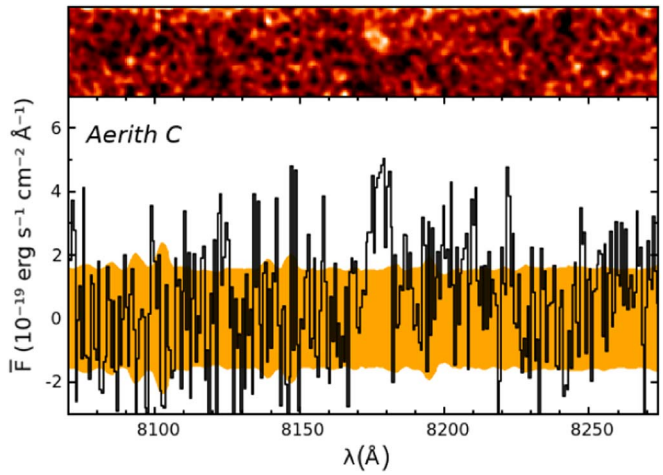

Figure 5. DEIMOS spectroscopy of Aerith C. No other lines are detected. The offset between the peak of z-band and NB816 emission (Figure 1) suggests the actual emission line flux is ∼9 times larger than that captured in the DEIMOS slit (see Section 2.3.3).

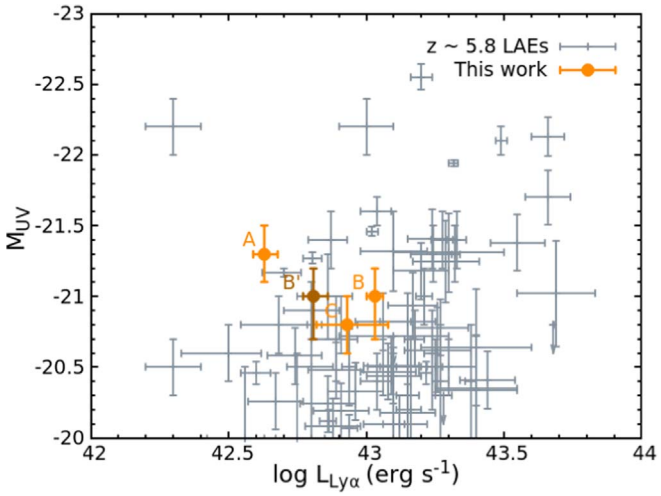

Figure 6. Comparison of the Lyα luminosities and M_{UV} of the proximate LAEs with other bright ($M_{UV} < -20$) galaxies at $z > 5.7$. Aerith A displays a relatively low $L_{Ly\alpha}$ for its M_{UV}, which could indicate a spectral slope harder than $\beta = -2$. The darker *B'* symbol indicates the properties of Aerith B if its blue Lyα peak had been absorbed by the IGM. The comparison sample is drawn from Shibuya et al. (2018), Mallery et al. (2012), Hu et al. (2010), Ouchi et al. (2008), Matthee et al. (2017), Ding et al. (2017), Jiang et al. (2013, 2018), and Higuchi et al. (2019), with some values presented in Harikane et al. (2019).

spectroscopically. This fraction is consistent with the detection originating entirely from scattered light from the offset NB816 source. Assuming that the UV and Lyα emissions are physically related, we measure $EW_{Ly\alpha} = 55^{+8}_{-5}$ Å; correcting for the systematic offset of the Lyα line, as for Aerith A, yields $z_{sys} = 5.722 \pm 0.004$ for an offset of $\Delta v = 166 \pm 107$ km s^{-1} (Erb et al. 2014).

No continuum is detected at the location of the offset NB816 detection in *B*, *V*, *r*, or *z*. A detection in the *i* band is consistent with originating entirely from the emission line captured in NB816. It is therefore likely that the totality of the NB816 flux originates in the emission line at $\lambda = 8176.9$ Å. If this were an Hα 6465 Å line at $z = 0.245$, we would expect the corresponding Hβ 4862 Å emission line to fall in the *r* broad band. No such detection is seen, with $F_r < 3.7 \times 10^{-18}$ erg s^{-1} cm^{-2}, implying a line ratio [Hα/Hβ] > 6.2 at 2σ. This is larger than those seen in nearly all Hα line emitters (e.g., Concas & Popesso 2019 and therein), thereby excluding the most common source of low-z interlopers.

A06 identified the NB816-only source as a separate, related component to the z detection. If the emission line at $\lambda = 8176.9$ is Lyα at $z = 5.7263$, the 6.3 pkpc physical offset between the z continuum and the emission line is in excess of any objects previously reported, even in the cases of very clumpy high-z galaxies (Carniani et al.2018) when the UV and dust continuum are frequently offset from each other (Maiolino et al. 2015; Carniani et al. 2017). Various mechanisms including inhomogeneous ionization are invoked at $z > 6.0$ to explain the offsets between continuum emission lines such as [C II] 158 μm and highly ionized nebular lines such as [O III] 5007 Å (Katz et al. 2019), but these offsets are $\leqslant$3 pkpc. Since the redshifts of the two components are consistent, another possibility is that there are two associated galaxies (potentially a galaxy merger) in which one member displays a very large Lyα/UV ratio and the other a very small ratio. We speculate that this could arise through an inhomogeneous/clumpy distribution of star formation and dust, as is sometimes seen in young galaxies (e.g., Carniani et al. 2018 and therein).

2.4. UV Magnitudes and Star Formation Rates

We calculate the UV magnitude M_{UV} assuming a flat spectral slope $\beta = -2$ and the *k*-correction $-2.5(\beta + 1)\log_{10}(1 + z_{Ly\alpha})$. M_{UV} can be related to the star formation rate (SFR) via SFR ($M_\odot$ yr^{-1}) $= 1.4 \times 10^{-28} L_{\nu,UV}$ (Kennicutt 1998) assuming a Salpeter initial mass function (IMF; Salpeter 1955). Alternatively, the SFR can be estimated within 15% from the properties of the Lyα emission line alone (Sobral et al. 2018; Sobral & Matthee 2019):

$$\mathrm{SFR}_{Ly\alpha}[M_\odot\ \mathrm{yr}^{-1}] = \frac{L_{Ly\alpha} \times 7.9 \times 10^{-42}}{(1 - f_{esc})(0.042 \times \mathrm{EW}_0)}, \quad (1)$$

where EW_0 is the equivalent width of the Lyα line in the rest frame, and a Salpeter IMF is again assumed. The resulting estimates of SFR are shown in Table 2 assuming $f_{esc} = 0.1$ for Aerith A and Aerith C, as measured in LAEs at later epochs (Verhamme et al. 2017; Fletcher et al. 2019). We use $f_{esc} = 0.05$ for Aerith B due to the results of the Lyα line fitting presented in Section 3. The $\sim 2\sigma$ disagreement between SFR_{UV} and $SFR_{Ly\alpha}$, with $SFR_{Ly\alpha} \simeq 2\ SFR_{UV}$, is common in $z \sim 5.7$ UV-selected LBGs with SFR $\lesssim 40\ M_\odot \mathrm{yr}^{-1}$ (e.g., Sobral & Matthee 2019 and therein). Additional uncertainty in the UV SFR could be due to a spectral slope harder than $\beta = -2$. The Lyα-derived SFR is dependent on the IMF; a Chabrier IMF (Chabrier 2003) results in predictions ∼2 times lower than with a Salpeter IM.

Both the M_{UV} and $L_{Ly\alpha}$ properties of our objects are typical of $z \sim 5.8$ galaxies for which both measurements are available (Figure 6). Interestingly, Aerith C displays a typical $L_{Ly\alpha}/M_{UV}$ ratio under the assumption that its UV and emission line components are related despite the 6.3 pkpc physical offset. Aerith A displays an $L_{Ly\alpha}$ about 0.5 dex lower than the median value at $z \sim 5.8$ given its UV magnitude. Its $L_{Ly\alpha}/M_{UV}$ ratio is comparable to the objects of Jiang et al. (2013), which possess

particularly steep UV continuum slopes ($\beta \leqslant -2$). This could be indicative of a young stellar population and/or lack of dust. We also note that most samples of LAEs at $z \sim 5.8$ are Lyα-selected rather than UV-selected, which creates a sampling bias to higher values of $L_{\mathrm{Ly}\alpha}$.

3. Aerith B: A Double-peaked LAE and Constraints on the Escape Fraction at $z \sim 6$

The most striking feature of the newly discovered proximate LAEs is the wide double-peaked Lyα emission line in Aerith B. Absorption by the partially neutral IGM makes this feature exceedingly rare at $z > 5$ (Hu et al. 2016; Songaila et al. 2018) and destroys the large amount of information on galactic properties it contains. However, Aerith B is located at a distance $D_{\mathrm{QSO}} < 912$ pkpc away from an $M_{\mathrm{UV}} = -27.75$ quasar (Bañados et al. 2016). The quasar's contribution to the local ionization field ($\Gamma_{\mathrm{H\,I}}$) is $\gtrsim$10 times larger than the radiation field of the galaxy itself and ~100 times stronger than the UVB at its peak at $z = 2$ (Becker et al. 2007; Bolton & Haehnelt 2007; Faucher-Giguère et al. 2008).

We show, in this Section, how this proximate LAE offers unique insight into the escape fraction of ionizing photons at $z \sim 6$.

3.1. Visibility of the Lyα Emission Line at $z > 5.5$

The Aerith B galaxy provides direct evidence that the $z > 5.5$ IGM is affecting the visibility of the Lyα line. This effect has been commonly argued to be responsible for the declining Lyα fraction in LBGs at $z > 6$ (Stark et al. 2010; Pentericci et al. 2014; Mason et al. 2018), the sharp decline of the LAE number density (Choudhury et al. 2015; Weinberger et al. 2018), and changes in the clustering of LAEs (Furlanetto et al. 2006; McQuinn et al. 2007; Ouchi et al. 2018).

The velocity separation between the peaks of Lyα in Aerith B is $\Delta v_{\mathrm{sep}} = 580 \pm 80$ km s^{-1}, comparable to the median for double-peaked $z \sim 3$ LAEs and for double-peaked $z \sim 0.3$ GPs (Figure 7). Interestingly, current surveys of LAEs at $z \sim 5.7$ are nearly all sensitive at this level, both in terms of S/N and spectral resolution. For example, 44 LAEs within a potential proto-cluster at $z \sim 5.7$ compiled by Harikane et al. (2019) were all observed with spectroscopic resolutions no worse than $\Delta v = 300$ km s^{-1}, and they have fainter $L_{\mathrm{Ly}\alpha}$ than Aerith B, but none were found to display a double-peaked Lyα line. Confusion with the [O II] 3727 Å doublet ($\Delta v = 224$ km s^{-1}) is potentially an issue for identifying the double Lyα peak at $z > 4.8$, but this is negligible in the regime of $\Delta v > 500$ km s^{-1}. At $2 < z < 3.2$, roughly 15%–25% of all LAEs display double-peaked Lyα lines at least as widely separated as this (Kulas et al. 2012; Trainor et al. 2015). Similarly, ~25% of $z = 0$ analogs posses such wide peak separations (Rivera-Thorsen et al. 2015; Yang et al. 2017). The lack of $\Delta v > 500$ km s^{-1} double-peaked LAEs detected at $z > 5.5$ compared to $z < 3$ is therefore likely due to reasons other than observational completeness, such as absorption by the IGM. It is still surprising that two double-peaked LAEs should be found outside of proximity zones at $z > 6.5$, but none at $5 < z < 6.5$, where the completeness is much higher.

The visibility of the Lyα blue peak in the $z > 6.5$ LAEs, NEPLA4 and COLA1, is speculated to arise from local "ionized bubbles" sourced by the galaxies themselves and/or an associated highly ionizing population (Matthee et al. 2018). However, both of those galaxies are significantly brighter than Aerith B and the galaxies in Harikane et al. (2019; Figure 7). Since Aerith B demonstrates that $z > 5.5$ LAEs do sometimes possess intrinsically double-peaked Lyα profiles, we conclude that moderately bright galaxies are not generally able to sustain their own significantly ionized bubbles even in the context of a $z \sim 5.7$ proto-cluster (Harikane et al. 2019).

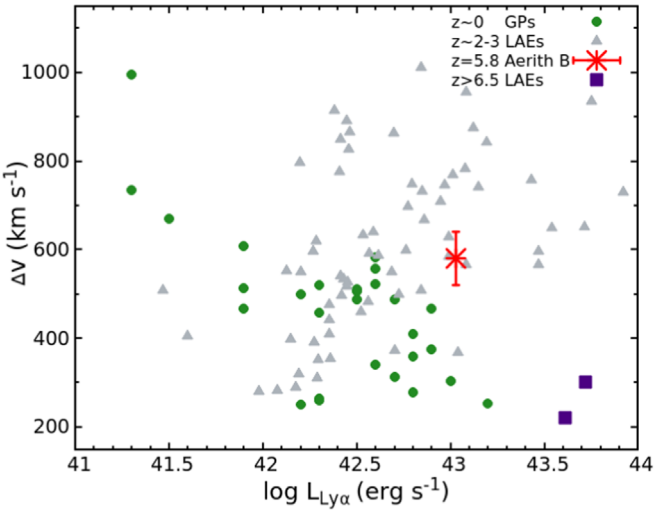

Figure 7. The red-blue peak velocity separation in Aerith B is consistent with the median seen in both $z \sim 2-3$ LAEs and $z \sim 0$ GP galaxies (Yang et al. 2017); although, the latter tend to be ~0.5 dex fainter in $L_{\mathrm{Ly}\alpha}$ at the same peak separation. The $z > 6$ double-peaked LAEs, COLA1 and NEPLA4, are outliers from both comparison samples. The $z \sim 2-3$ sample is drawn from Yamada et al. (2012), Hashimoto et al. (2015), and Vanzella et al. (2016). $L_{\mathrm{Ly}\alpha}$ values from Kulas et al. (2012) have been adjusted to reflect a Salpeter IMF rather than Chabrier.

3.2. Ionizing Escape Fraction

The Lyα peak separation is a highly sensitive tracer of the ionizing escape fraction, well calibrated on studies of $0 \leqslant z \leqslant 3$ galaxies with detections of LyC emission (Jaskot & Oey 2013; Hayes 2015; Izotov et al. 2018). Theory predicts the preferential escape frequency of Lyα photons and, thus, the peak separation to be governed by the H I column density (Adams 1972; Neufeld 1990). The wide Lyα peak separation favors a low f_{esc}(LyC). If we adopt the empirical fitting formula of Izotov et al. (2018),

$$f_{\mathrm{esc}}(\mathrm{LyC}) = 3.23 \times 10^4 \Delta v_{\mathrm{sep}}^{-2} - 1.05 \times 10^2 \Delta v_{\mathrm{sep}}^{-1} + 0.095, \quad (2)$$

then for the measured peak separation of Aerith B $\Delta v_{\mathrm{sep}} = 580 \pm 80$ km s^{-1}, we find an LyC escape fraction

$$f_{\mathrm{esc}}(\mathrm{LyC}) \approx 0.01 \ \text{(for Aerith B } z \simeq 5.79). \quad (3)$$

Samples at $z < 3$ contain only modest numbers of LAEs with peak separations $\Delta v > 400$ km s^{-1} followed up to detect LyC leakage at the ~1% level. This is partially because these galaxies are selected through pre-existing signs of high ionization (e.g., Izotov et al. 2016a, 2016b). Scatter is therefore challenging to estimate; we note that 100% (5/5) of galaxies with $\Delta v > 400$ km s^{-1} Lyα peak separation have $f_{\mathrm{esc}} < 10\%$. However, simulations indicate that such a wide peak separation corresponds to the absence of low ($N_{\mathrm{HI}} < 10^{17}$ cm^{-2}) column density channels in the system (Kakiichi & Gronke 2019; Kimm et al. 2019) and, therefore, little to no escape of ionizing photons.

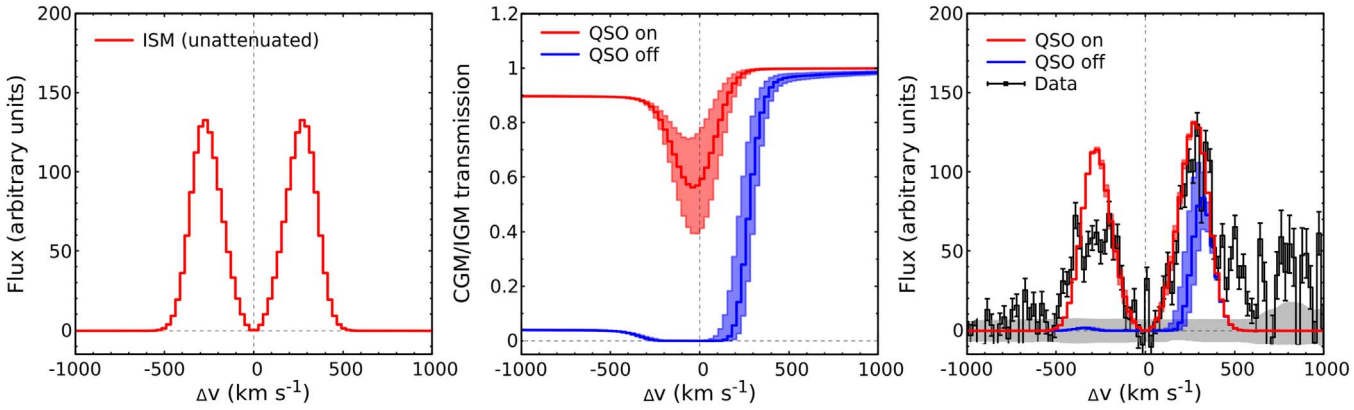

Figure 8. CGM attenuation of the Lyα double peak in Aerith B. Left panel: intrinsic Lyα emission in the galaxy's ISM. Middle panel: attenuation curves including the effect of Aerith B's CGM and IGM transmission resulting from J0836 and its clustered galaxy population (red) and the expected IGM attenuation in the absence of a luminous quasar (blue). The width of the lines span CGM parameters $r_{\rm min}$ = 10, 20, 50 pkpc (Section 3.4). Right panel: resulting observed Lyα emission line structure, with observations shown in black, and the models colors the same as those in the middle panel.

In contrast, the double-peaked Lyα emission of COLA1 at $z = 6.59$ has a separation $\Delta v_{\rm sep} = 220 \pm 20$ km s^{-1}, indicating (Matthee et al. 2018):

$$f_{\rm esc}\,({\rm LyC}) \approx 0.29 ({\rm for\ COLA1}\ z \simeq 6.59). \quad (4)$$

The narrow peak separation in COLA1 indicates the presence of low column density channels through which ionizing radiation can escape, but high enough ($>10^{14}$ cm^{-2}) that scattering of Lyα photons can still take place at the core of the system. The difference between the Lyα lines in Aerith B and COLA1 and NEPLA4 highlights that a variety of escape fractions are present at the tail end of reionization. The low $f_{\rm esc}$ in Aerith B is unlikely to be due to viewing angle, as simulations predict that Lyα peak separations $\Delta v > 300$ km s^{-1} require a significant absence of ionizing channels (Kakiichi & Gronke 2019). Rather, the difference could be due to intrinsic luminosity and/or clustering, with COLA1 and NEPLA4 being 0.5 dex brighter than Aerith B and potentially residing in ionized bubbles that they contribute to sustaining.

The flux ratio between the two peaks of Lyα in Aerith B, $A = F_{\rm blue}/F_{\rm red} = 0.65 \pm 0.05$, is in good agreement with the $A/W_{{\rm Ly}\alpha}$ relation suggested by Erb et al. (2014). We are able to accurately obtain the systemic redshift of Aerith B by using the flux minimum in between the two Lyα peaks, which traces the gas responsible for scattering. Indeed, the offset between this point and the peak of Lyα emission is $\sim$250 km s^{-1}, in agreement with lower-z results. $F_{\rm blue}/F_{\rm red} \neq 1$ is indicative either of attenuation by the CGM and IGM, or an outflowing shell of material (Bonilha et al. 1979), or more likely both (Figure 8). In order to extract further physical information on the galaxy, we must disentangle these effects.

3.3. CGM and IGM Attenuation of the Line

How much of the peak asymmetry in Aerith B could be due to CGM and IGM attenuation? Cross-correlation measurements between LAEs and the Lyα forest in multiple quasar fields (Meyer et al. 2019b, 2019c) show evidence for CGM attenuation of Lyα transmission around LAEs (or related metal tracers) on $\lesssim$1 pMpc scales at $z \sim 6$.

We model the effect of CGM attenuation as follows. The transverse Lyα absorption by the CGM links the mean line-of-sight effective optical depth $\tau_{\rm eff}^{{\rm Ly}\alpha}$ to the Lyα emission line of a galaxy schematically via (Kakiichi & Dijkstra 2018),

$$\tau_{\rm eff}^{{\rm Ly}\alpha}(\nu_e, r_\perp) \propto \int_{-\infty}^{\infty} dv \int_0^{\infty} dN_{\rm HI} f(N_{\rm HI})[1 + \xi_\nu(v, r_\perp)][1 - e^{-\sigma_\nu N_{\rm HI}}], \quad (5)$$

with $\sigma_\nu = \sigma_\alpha \phi_V[\nu_e(1 - v/c)]$ where ϕ_V is the Voigt profile, $f(N_{\rm HI})$ is the H I column density distribution function, and $\xi_\nu(v, r_\perp)$ is the velocity-space correlation function between galaxies and Lyα absorbers. The interested reader can refer to the original paper for details. Two parameters choices are important, as the CGM absorption depends on the average velocity scatter of the absorbing gas (σ_α) and the innermost radius of CGM absorption $r_{\rm min}$. We arbitrarily fix σ_α to an typical value for low-z LAEs of 100 km s^{-1} (Gronke 2017). $r_{\rm min}$ characterizes the transition from small-scale, galactic processes through which Lyα emission is produced and scattered into the line of sight, to the CGM regime where Lyα photons are scattered out of the line of sight (Laursen et al. 2011). In this regime, absorption can be modeled by analytic or semi-numeric means (Kakiichi et al. 2016). The radius of transition is of the order of $\sim 1.5 r_{\rm vir}$, the halo's virial radius. The halo mass of Aerith B is estimated to be around $\sim 10^{11} M_\odot$ (see discussion in Section 5.1), which corresponds to a virial radius of $\sim$20 pkpc at $z = 5.8$. We therefore produce a range of curves for $r_{\rm min} = 10, 20,$ and 50 pkpc, resulting in the uncertainty in CGM absorption shown in the middle panel of Figure 8. Values larger than 50 pkpc result in asymptotically less CGM absorption.

We set the normalization of $f(N_{\rm HI})$ by requiring $e^{-\tau_{\rm eff}^{{\rm Ly}\alpha}(\nu_e)}$ to asymptotically approach $\langle e^{-\tau_\alpha(r_\perp, r_\parallel)} \rangle$ bluewards of the line center in order to recover the correct limit of IGM attenuation. The resultant $e^{-\tau_{\rm eff}^{{\rm Ly}\alpha}(\nu_e)}$ then gives the mean estimate of the CGM +IGM attenuation curve around the Lyα emission line of a galaxy.

The CGM+IGM attenuation curve near the Lyα line profile at the position of Aerith B, as indicated in Figure 8, shows that the strong ionizing radiation field (ΓH I $\sim 10^{10}$ s^{-1}) from the quasar is needed to raise the blue transmission of the Lyα line. The attenuation due to the CGM+IGM is insufficient to account for the large peak asymmetry (Figure 8, right panel),

indicating that an outflow structure is present, as is commonly seen in LAEs at $2 < z < 3$ (Steidel et al. 2010; Gronke 2017).

3.4. Modeling of the Lyα Emission Line with a Shell Model

The outflowing shell model offers a powerful way to extract galaxies' properties from their Lyα emission morphology. Using the CGM+IGM attenuation curve we just derived, we can now fit the Lyα emission profile of Aerith B with such an outflowing shell. Although the exact physical meaning of the shell model is still under debate (Gronke et al. 2017; Orlitová et al. 2018), it provides a quick way to extract properties of the scattering medium from Lyα spectra. Furthermore, it also accounts for bulk motions affecting, e.g., the asymmetry of the Lyα emission line, and is thus more sophisticated than simply measuring the peak separation as was done earlier.

In this simple model, an Lyα and continuum-emitting source is surrounded by a dense shell of gas and dust outflowing at constant velocity (Ahn et al. 2003). The shell model successfully captures most of the diversity of Lyα emission line profiles at both $z \sim 0$ (Yang et al. 2017) and $1 < z < 3$ (Verhamme et al. 2008, 2015; Karman et al. 2017). It consists of at least five free parameters: the bulk velocity $v_{\rm exp}$ (positive for an outflow), the column density of neutral hydrogen $N_{\rm H\,I}$, the gas temperature T, the intrinsic width of Lyα emission σ_i, and the optical depth of dust τ_d.

The modeling and fitting is conducted as in Gronke et al. (2015) and Gronke (2017). The CGM+IGM attenuation curves discussed in Section 3.3 are applied to reconstruct the Lyα profile before absorption. In addition to the parameters listed above, we fit the intrinsic equivalent width of the Lyα emission line before absorption ($\rm EW_i$). The galaxy redshift (z) is allowed to vary to optimize the fit; we imposed a Gaussian prior on the systemic redshift $z_{\rm sys}$ with $(\mu, \sigma) = (5.793, 0.003)$ based on the observations that we truncate at 3.5σ. We refer the interested reader to the two papers above for technical details.

The curves resulting from the best-fit parameters are shown in Figure 9, compared to the observed spectrum. We estimate parameter uncertainties by using the 85th percentiles of the posterior parameter distributions, and we include the uncertainty on the choice of CGM parameter $r_{\rm min}$ by running three separate fits for $r_{\rm min} = 10$, 20, and 50 pkpc and taking the envelope of the resulting parameter constraints. This yields a hydrogen column density $\log(N_{\rm H\,I}/{\rm cm}^{-2}) = 19.3^{+0.8}_{-0.2}$, which is typical of $2 < z < 3$ LAEs studied similarly in Gronke (2017). The best-fit outflow velocity $v_{\rm exp} = 16^{+4}_{-11}$ km s^{-1}, intrinsic velocity scatter $\sigma_i = 235^{+42}_{-17}$ km s^{-1}, and gas temperature $\log T/K = 3.8^{+0.8}_{-0.7}$, are all typical parameters within 1σ of those found in lower-z LAEs. We note that this is not driven by the uncertainties on Aerith B's properties, which are ∼2–3 times smaller than the intrinsic scatter seen among lower-z objects. The only exception is the dust temperature, $\tau_d = 2.27^{+2.29}_{-2.20}$, whose uncertainty spans the entire range of values observed in $2 < z < 3$ analogs. We believe this is due to degeneracies with CGM attenuation.

Physical effects beyond our modeling may temper the accuracy of the shell-model fit. For example, the best-fit intrinsic dispersion σ_i is a factor ∼2 larger than the velocity dispersion of the absorbing gas that we assumed in Section 3.3. Ideally, the IGM+CGM attenuation should be modeled at the same time as the outflow. Due to its high column density and extreme external ionization, it is also possible that some of the Lyα emission in Aerith B comes from Lyα fluorescence, which is beyond the scope of our modeling (but see discussion in Section 5.3). Our objective was to directly compare the results of the shell-model fitting to the analysis at $2 < z < 3$ in Gronke (2017) by using the same methodology. In conclusion, we found that the physical parameters extracted from Aerith B via shell-model fitting are strikingly similar to those seen in $2 < z < 3$ LAEs in all respects.

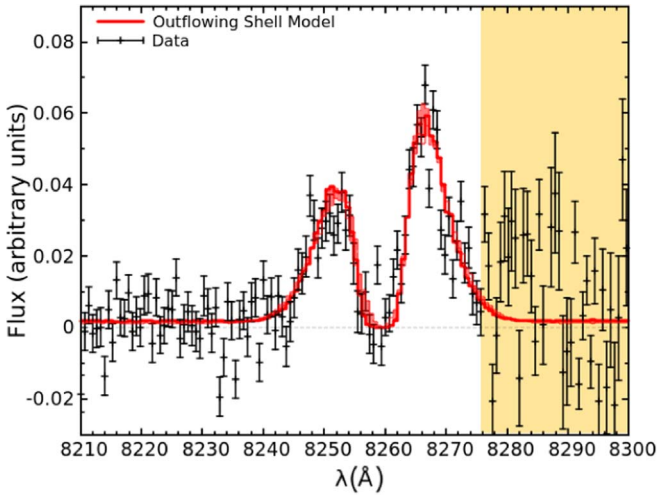

Figure 9. Extracted flux of the double-peaked Lyα emission line of Aerith B (black). The peak separation rules out significant LyC leakage. The width of the red line represents the fit uncertainty arising from CGM attenuation, corresponding to the middle panel of Figure 8 (see Section 3.4).

3.5. Correspondence with Lyα Forest Absorption and Metallicity

Aerith B appears to coincide in redshift with an Lyα absorber inside J0836's proximity zone (Figure 10). Using a high-resolution HIRES (Vogt et al. 1994) spectrum of J0836 first presented in Bolton et al. (2011), we fit this absorber with a Voigt profile using `vpfit` (Carswell & Webb 2014). We obtain a column density $\log N_{\rm H\,I} = 14.71 \pm 0.05$, too low to constitute a Lyman-limit system (which would require $\log N_{\rm H\,I} < 17.2$; e.g., Cooper et al. 2019). By using the larger wavelength coverage of the X-Shooter spectrum, we search the expected locations of common metal absorbers, finding none. Metallicity limits are obtained by inserting increasingly strong absorbers at those wavelength locations until the features exceed the spectrum uncertainty (Bosman et al. 2017). We find abundances $[{\rm Si/H}] \lesssim -0.01$ and $[{\rm C/H}] < -0.2$ at 2σ, consistent with low enrichment up to solar. This is consistent with expectations for weak H I absorbers at $z > 3$ (e.g., Fumagalli et al. 2016).

The distance between the sightline and Aerith B ($D_\perp = 334$ pkpc) is probably too great for this absorber to be associated with the galaxy's CGM (but see Rudie et al. 2012). However, the feature could be associated with a larger-scale structure such as a gas inflow/outflow, or the CGM of a clustered fainter galaxy.

4. J0836's Proximity Zone

We now demonstrate that a further valuable aspect of locating proximate LAEs is their utility in constraining the extent and structure of the ionized proximity zones. The transverse proximity effect detected toward Aerith A, the strength of the ionization field at the location of Aerith B, and the redshift alignment between Aerith C and the end of the proximity zone, all offer information

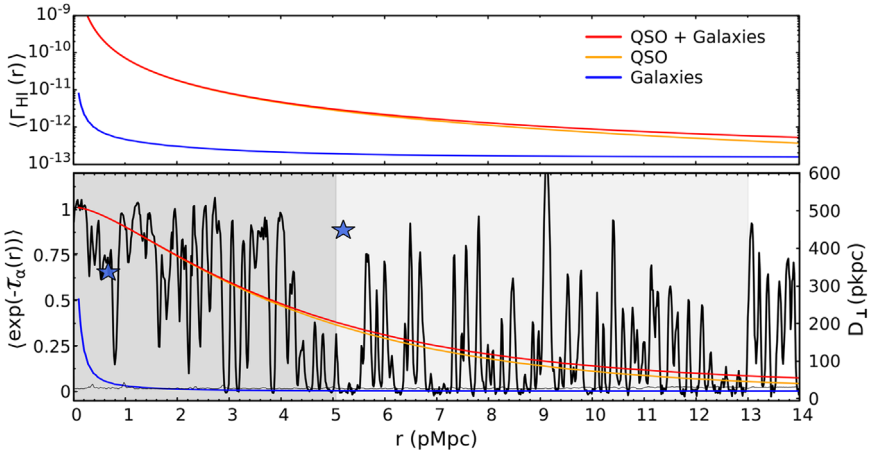

Figure 10. Comparison of the continuum-normalized X-Shooter spectrum of J0836 (black) with the theoretical model of line-of-sight Lyα absorption toward the quasar. The model shows the contributions to (top panel) the photoionization rate and to (bottom panel) the Lyα transmission inside the quasar proximity zone, caused by the luminous quasar itself ($M_{\rm UV} = -27.75$, orange) and sub-luminous $M_{\rm UV} > -15$ galaxies clustered around the central quasar (blue). The total effect is indicated in red. The locations of Aerith B and C are indicated with stars, and the right-hand-side y-axis gives the angular distance $r_\perp$ in proper units. The reported proximity zone sizes by Eilers et al. (2017) of 5.06 pMpc (dark shaded region) and by Carilli et al. (2010) of 13.0 pMpc (light shaded region) are also shown.

on the propagation of ionizing photons from the AGN. Specifically, the observed properties of the proximate LAEs are sensitive to the quasar's opening angle, lifetime or variability, and to the thermal and density profiles of the surrounding IGM. In this section, we model the impact of these various parameters on J0836's proximity zone together with the Lyα emitting galaxies in its environment. We closely follow the methodology introduced in Kakiichi et al. (2018), but we extend it to include the quasar radiation field and the visibility of the Lyα line in proximate LAEs.

4.1. Quasar Opening Angle

A quasar shines with an ionizing photon production rate $\dot{N}_{\rm ion}^{\rm QSO}(t)$. Using the published broadband magnitudes of J0836, we measure a spectral slope $\beta = -1.4 \pm 0.1$ (Section 5.1) that is consistent with the traditional value of the far-UV spectral energy distribution of quasars, $L_\nu \propto \nu^{-1.5}$ for $\lambda < 1050$ Å (Telfer et al. 2002). This corresponds to $\dot{N}_{\rm ion}^{\rm QSO}(0) = 3.8 \times 10^{57}$ s^{-1}. We assume that the quasar is radiating in a bipolar cone with an opening angle $\theta_{\rm Q}$. The photoionization rate from the quasar in the observed frame is then zero outside the cone, and

$$\Gamma {\rm H\,I}^{\rm QSO}(r_\parallel, r_\perp) = \frac{-\beta\sigma_{912}}{3-\beta}\frac{\dot{N}_{\rm ion}^{\rm QSO}[-\Delta t(r_\parallel, r_\perp)]}{4\pi(r_\parallel^2 + r_\perp^2)} \quad (6)$$

within the cone, where σ_{912} is the photoionization cross section at the Lyman limit, and Δt is the time lag at a distance $(r_\parallel, r_\perp)$ from J0836. The distance $r_\parallel$ is the line-of-sight proper distance from the quasar with a positive sign toward the observer, and $r_\perp$ is the perpendicular separation along the plane of sky.

The uncertainty on the redshift of the quasar makes the geometry of the system unclear. The best-fit locations of both sources put Aerith B slightly in front of the quasar, at an opening angle of $\theta = 80°$. At 1σ, the galaxy could also be located further away toward the observer with $\theta = 21°$ or even behind the quasar at $\theta = 25°$. However, we have argued in the previous Section that the visibility of a blue Lyα peak in Aerith B requires a high-Lyα transparency of the IGM at its location of at least $\langle e^{-\tau_\alpha(r_\perp^B, r_\parallel^B)}\rangle \approx 80\%$ transmission.

This necessitates that the galaxy be included within the opening angle of the quasar, which must therefore conservatively be larger than

$$\theta_{\rm Q} > \arctan\left(\frac{r_\perp^B}{r_\parallel^B}\right) \gtrsim 21°, \quad (7)$$

if the central axis of the bipolar cone is directly pointing toward us, with a strict lower bound $\theta_{\rm Q} > 10°$, if we are observing the quasar exactly along the edge of the cone. We are unable to put an upper limit on the opening angle. The other two proximate LAEs, Aerith A and C, are located much closer to the line of sight, at angles $\lesssim 5°$. Given that J0836 is a very radio-loud quasar (Frey et al. 2005), presumably with a jet, we may be observing it closer to the central axis since local observations indicate small intrinsic opening angles of AGN jets with a median of $\theta_{\rm jet} = 1.^\circ3$ (Pushkarev et al. 2017). Thus, we take $\theta_{\rm Q} \geqslant 21°$ as a fiducial constraint.

4.2. Quasar Timescale

Quasars accreting at or above the Eddington limit, such as J0836 (Kurk et al. 2007), often display variability in brightness. The production rate of ionizing photons, and in turn the opacity of the surrounding IGM, will react to AGN variability with a time lag depending on the properties of the IGM and distance from the quasar. Quasar flickering can thus create an ionization "echo" in its surroundings. It has long been proposed to use this effect to accurately time the past radiative activity of luminous quasars by using the Lyα opacity toward background sources at small impact parameters (Adelberger 2004; Hennawi et al. 2006; Visbal & Croft 2008; Schmidt et al. 2019). We are now in a position to attempt such a measurement in practice. In J0836, we know that the ionizing radiation has reached the location of Aerith B but likely not the location of the slightly more distant Aerith A behind the quasar.

According to the above estimate of the quasar opening angle, Aerith A is indeed located within the bipolar cone region unless we are observing J0836 off-axis by more than $>9.^\circ7$, which seems disfavored by its radio-loud nature. Despite this, no continuum is detected immediately bluewards of the Lyα

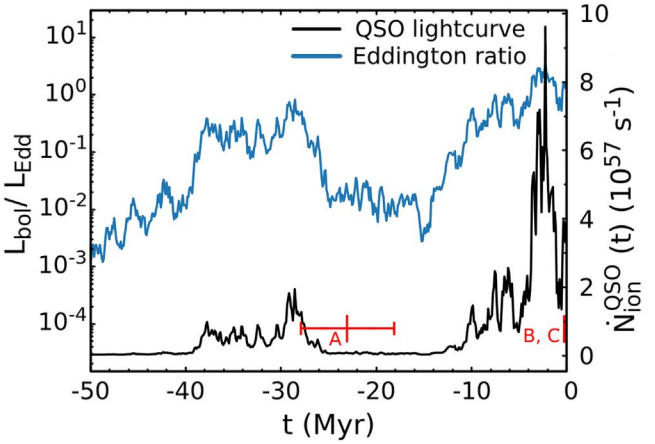

Figure 11. A simulated realization of J0836's light curve over the last 50 Myr: (left y-axis: blue) the time-variable Eddington ratio $L_{\rm bol}(t)/L_{\rm Edd}$ and (right y-axis: black) the ionizing photon production rate $\dot{N}_{\rm ion}^{\rm QSO}(t)$ as a function of time. $t = 0$ corresponds to the time at the quasar redshift $z = 5.795$ so that negative values indicate activity at earlier times. The vertical lines (red) mark the time delay surface at the locations of Aerith A, B, and C.

emission line in the object's spectrum, despite the fact that the redwards continuum is detected at 5.3σ (Section 2.3.1). To determine if this is significant, we must establish (i) the ionization propagation time lag as a function of distance from the AGN, and (ii) the expected transmission in Aerith A if the quasar had been on indefinitely.

To illustrate the effect of quasar variability, we implement luminosity variations of J0836 into our model using the variable accretion rate shown in blue in Figure 11. It is thought that strong radiatively driven feedback can halt and regulate the gas fueling the central accretion disk or onto the host galaxy (e.g., Novak et al. 2011; Hopkins et al. 2016). We follow the phenomenological stochastic model of quasar variability by Kelly et al. (2009; see also Kelly et al. 2014; Sartori et al. 2018), which assumes that the quasar light curve is a realization of damped random walk (or Ornstein–Uhlenbeck process; Uhlenbeck & Ornstein 1930). We describe the time evolution of the Eddington ratio as

$$d\log\frac{L_{\rm bol}(t)}{L_{\rm Edd}} = \left[\left\langle \log\frac{L_{\rm bol}}{L_{\rm Edd}}\right\rangle - \log\frac{L_{\rm bol}(t)}{L_{\rm Edd}}\right]\frac{dt}{\tau} + \sigma_{\rm E}\,dW(t), \quad (8)$$

where $dW(t)$ is the Gaussian random process, and the three parameters, $\langle \log L_{\rm bol}/L_{\rm Edd}\rangle$, $\sigma_{\rm E}$, and τ, correspond to the mean $\log L_{\rm Edd}$, its variability amplitude, and the timescale of variation, respectively. For simplicity, we assume illustrative values of $\langle \log L_{\rm bol}/L_{\rm Edd}\rangle = -2$, $\sigma_{\rm E} = 0.4$, and a characteristic variability timescale of $\tau = 10^7$ yr. We take $t = 0$ to refer to the time at which J0836 is observed leading to $\dot{N}_{\rm ion}^{\rm QSO}(t) \propto L_{\rm bol}(t)/L_{\rm Edd}$ being normalized at $z = 5.795$. The response of the quasar luminosity to this varying accretion rate is shown in Figure 11 (black). The time variability gives rise to a "layered" photoionization structure around the quasar as a function of line of sight and perpendicular separations indicated in Figure 12, which is directly traceable via the Lyα emission and absorption features of the proximate LAEs and along the line-of-sight absorption of J0836. An animated rendition of the ionization structure with successive variability histories can be found in the online version of Figure 12.

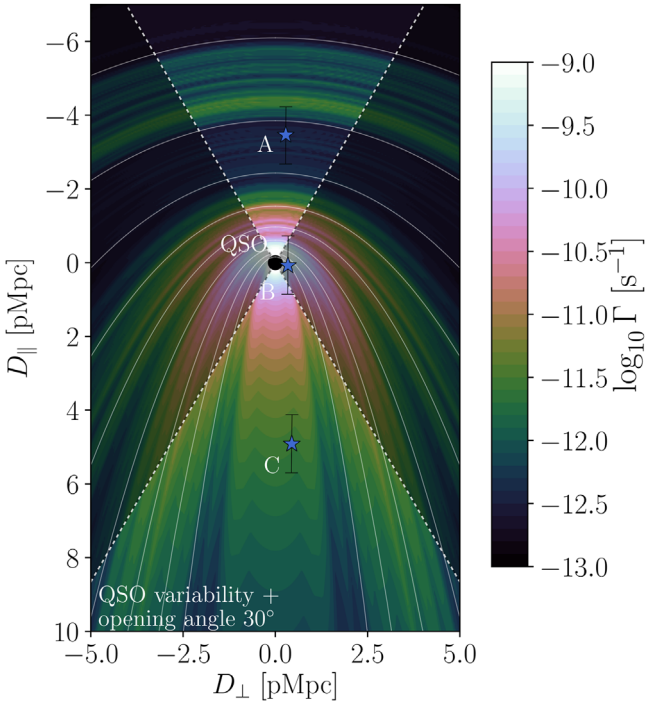

Figure 12. Two-dimensional representation of the photoionization rate from the quasar in the observed frame. The model corresponds to the light curve presented in Figure 11 with a biconical opening angle $\theta_{\rm Q} = 30°$. The black shaded region indicates the obscured region with $\Gamma{\rm H\,I}^{\rm QSO} = 0$, but isotropic emission is shown to more easily illustrate the apparent ionizing structure with time delay surfaces. The white contours indicate time delays of $\log(\Delta t/{\rm yr}) = 6.0, 6.2, 6.4, 6.6, 6.8, 7.0, 7.2, 7.4, 7.6$ from inside to outside. The quasar is marked with a circle, and the locations of Aerith A, B, and C relative to the quasar are marked with stars (the relative separations between the LAEs are not correctly captured in this 2D representation). The animated figure shows a timelapse of the ionization structures that would have been observed at different times in the past, based again on the evolution presented in Figure 11.
(An animation of this figure is available.)

We now model the radiation field resulting from this light curve following the methodology of Kakiichi et al. (2018). The local ionizing background inside the proximity zone includes a contribution from the quasar and from galaxies clustered around the central quasar host (detected and undetected). The ionizing power of the three detected galaxies is given by

$$\Gamma{\rm H\,I} \approx 4.8\times10^{-14}\left(\frac{r}{100\ {\rm pkpc}}\right)^{-2} \times\left(\frac{f_{\rm esc}^{\rm LyC}}{0.01}\right)\left(\frac{\rm SFR}{20\,M_{\odot}\ {\rm yr}^{-1}}\right){\rm s}^{-1} \quad (9)$$

assuming an ionizing emissivity $\xi_{\rm ion} = 10^{25.2}$ erg^{-1} Hz. This is a negligible fraction of the collective UVB contribution from the many faint galaxies located more than a few virial radii outside of the host haloes of the LAEs. Therefore, we can write the total photoionization rate in the quasar's environment as

$$\Gamma{\rm H\,I}(r_{\perp}, r_{\parallel}) = \Gamma{\rm H\,I}^{\rm QSO}(r_{\perp}, r_{\parallel}) + \langle\Gamma{\rm H\,I}^{\rm GAL,CL}(r_{\perp}, r_{\parallel})\rangle, \quad (10)$$

where $\Gamma{\rm H\,I}^{\rm QSO}$ and $\langle\Gamma{\rm H\,I}^{\rm GAL,CL}\rangle$ are the photoionization rates from the quasar and faint (undetected) galaxies surrounding it, respectively.

We compute the average expected value of the photoionization rate due to clustered galaxies using the conditional luminosity

function-based Halo Occupation Distribution (HOD) framework (Kakiichi et al. 2018). There have been suggestions of an over-density of galaxies around J0836 (Z03, A06), indicative of a massive dark matter halo in a biased region. We assume a quasar-host halo mass of $M_h > 10^{12.5} h^{-1} M_\odot$ and that only the central galaxy is undergoing quasar activity The ionizing parameters of the clustered galaxy population are fixed as $\langle f_{\rm esc}\xi_{\rm ion}\rangle = 0.10 \times 10^{25.2}$ erg^{-1} Hz, with a limiting magnitude of contributing galaxies $M_{\rm UV}^{\rm lim} = -15$ (Kakiichi et al. 2018).

We find that the contribution of galaxies to the total UV ionization field around the quasar is very sub-dominant to the ionizing radiation from the bright quasar itself even in the central regions (Figure 10). This is consistent with the view that although quasars turn on in biased environments pre-ionized by galaxy over-densities, once the central galaxy undergoes quasar activity, it outshines the surrounding galaxies and dominates the local photoionization rate during the quasar lifetime (Lidz et al. 2006). Clustered galaxies could still affect the morphology of the proximity zone through higher-order effects not included in our modeling. For example, the increased mean free path of ionizing photons within the biconical ionized region should boost the ionizing power of clustered galaxies in the volume (Davies 2020), which could potentially modulate the transverse extent of the proximity zone perpendicularly to the cone. This motivates the search for associated galaxies in large areas around quasars with extended proximity zones.

We are now in a position to calculate the time delay seen by each of our three proximate LAEs. If we define $t = 0$ to be the time when the light from the quasar reaches the observer, the observed radiation field at each point in space is sensitive to the quasar luminosity emitted at an earlier time with a time delay Δt given by

$$\Delta t = \frac{(r_\parallel^2 + r_\perp^2)^{1/2} - r_\parallel}{c}. \tag{11}$$

At the location of the Aerith galaxies, the visibility of the Lyα emission line is sensitive to

1. $\Delta t = 2.3 \pm 0.5 \times 10^7$ yr for Aerith A;
2. $\Delta t = 9.1\ ^{+41}_{-7.0} \times 10^5$ yr for Aerith B;
3. $\Delta t = 6.6\ ^{+1.3}_{-1.0} \times 10^4$ yr for Aerith C;

before the time corresponding to J0836's redshift of $z = 5.795$ (i.e., $t = 0.97$ Gyr after the Big Bang). As Aerith A is located behind the quasar, so by using it as a background source, we can use the Lyα forest along its sightline to probe the quasar activity between $t = -2.3 \times 10^7$ yr and $t = 0$.

Finally, we compute the expected mean Lyα absorption along the line of sight and transverse directions by convolving the Lyα opacity with the probability distribution function of density fluctuations Δ_b, $P_V(\Delta_b)$ (Pawlik et al. 2009);[7]

$$\langle \exp(-\tau_\alpha(r_\perp, r_\parallel))\rangle = \int d\Delta_b P_V(\Delta_b) \exp\left[-\tau_0 \Delta_b^\beta \left(\frac{\Gamma {\rm H\,I}(r_\perp, r_\parallel)}{10^{-12}\ {\rm s}^{-1}}\right)^{-1}\right], \tag{12}$$

[7] We note that the peculiar relative velocity between the IGM gas and the quasar as well as the redshift uncertainties modify the signal along the lines of sight, introducing the redshift-space distortions. The redshift evolution further introduces a line-of-sight asymmetry to the 2D Lyα absorption map. These are the higher-order effects that we ignore for simplicity.

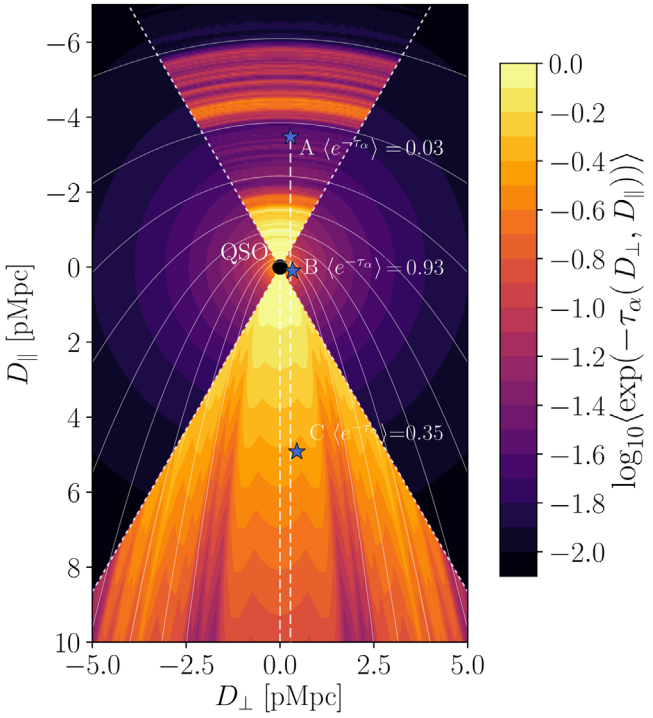

Figure 13. Same as Figure 12 but showing the simulated level of Lyα opacity $\langle \exp(-\tau_\alpha)\rangle$ inside J0836's proximity zone as a function of the line of sight and perpendicular distances to the quasar. The model includes both the ionizing contributions from the quasar and galaxies surrounding it.

where $\beta = 2 - 0.72(\gamma - 1)$,

$$\tau_0 \simeq 2.2(1 + \chi_{\rm He})\left(\frac{T_0}{10^4\ {\rm K}}\right)^{-0.72}\left(\frac{1+z}{5}\right)^{9/2} \tag{13}$$

is the optical depth evaluated at mean density (e.g., Becker et al. 2015a), $\Gamma {\rm H\,I} = 10^{-12}\ {\rm s}^{-1}$, and $\chi_{\rm He}$ is the fraction of electrons released by singly ionized ($\chi_{\rm He} \simeq 0.0789$) and doubly ionized ($\chi_{\rm He} \simeq 0.158$) Helium. Based on the measurement from the Doppler widths of Lyα absorption lines in J0836, we assume a uniform ($\gamma = 1$) temperature at $T_0 = 1.8 \times 10^4$ K (Bolton & Haehnelt 2013) and that the helium is doubly ionized. This gives an estimate of the typical proximity zone Lyα absorption profile of $z \simeq 5.8$ quasars with $M_{\rm UV} = -27.75$ averaged over many realizations of density fluctuations, shown in Figure 10. Clearly, an observed spectrum is modulated around this mean profile because of the fluctuations. In Figure 13, we show the resulting 2D Lyα transmission structure inside J0836's proximity zone using the illustrative light curve in Figure 11.

In conclusion, we find that if the quasar were active long enough, its radiation field would raise the CGM+IGM transmissivity at the location of Aerith A to $T \simeq 55\%$. The observed lack of continuum transmission immediately blueward of Lyα is in mild tension with this prediction ($T < 23\%$ over $8305 < \lambda < 8320$ Å at 1σ) but still marginally permitted at $\sim 2.4\sigma$. In addition, $T = 55\%$ would be sufficient to confidently detect a possible blue peak of the Lyα emission line, if it were present and similar to Aerith B's. Therefore, J0836's latest quasar phase has likely not lasted long enough to ionize the surroundings of Aerith A. This implies the recent

active luminous quasar phase has lasted for

$$2.1 \times 10^5 \text{ yr} < t_{\text{age}} < 2.8 \times 10^7 \text{ yr}, \quad (14)$$

where the lower bound is given from the presence of a double-peak Lyα line in Aerith B. If Aerith B is located behind the quasar, as permitted by the redshift uncertainties within 1σ, the bounds on quasar phase triggering timescale would be significantly tighter. A better redshift determination for J0836 is needed to refine these results.

In the past, the quasar duty cycle has been estimated via abundance matching with their dark matter halo masses, which are in turn estimated from the clustering properties of quasars (e.g., Haiman & Cen 2001). The resulting constraints, $10^6 \text{ yr} < t_{\text{age}} < 10^9 \text{ yr}$, are weak yet consistent with our measurement (White et al. 2012; Conroy & White 2013; Cen & Kimm 2015). We are also in agreement with Eilers et al. (2017), who estimate an average quasar episodic lifetime of $t \sim 10^6$ yr at $z \sim 6$ based on the occurrence rate of quasars with very short proximity zones. We discuss the implications of this quasar lifetime on the formation of SMBHs in Section 5.2.

4.3. Extent and Structure of the Proximity Zone

In Figure 10, we compare the observed continuum-normalized spectrum of J0836 with the Lyα absorption model along the sightline of the quasar. We find that the observed proximity zone size of J0836 (Eilers et al. 2017) is small for the brightness of the quasar. The boundary of the proximity zone is coincident with the location of the foreground LAE Aerith C $\simeq$5 pMpc in front of the quasar. In addition, the amount of transverse transmission observed over the narrowband imaging toward Aerith A is consistent with the prediction from our model ($\tau_{\text{NB}} = 1.2^{+0.4}_{-0.3}$). Together, this evidence suggests that J0836's proximity zone is prematurely truncated by an intervening density fluctuation. Since the transverse separation of Aerith C to the quasar is 446 ± 8 pkpc, this absorption is unlikely to arise from the galaxy's CGM or even inflows. However, we note that Aerith C appears to consist of two components with different Lyα EWs (Section 2.3.3). We suggest that the galaxy (or galaxies) may be tracing a larger-scale over-density responsible for absorption along the line of sight, truncating the proximity zone. Indeed, the following dip below 10% of the continuum in J0836's Lyα forest occurs at 13 pMpc, as identified by Carilli et al. (2010). This size would be in close agreement with the model expectation and would be the largest proximity zone ever observed.

5. Discussion

5.1. Lack of Quenching

Early quasars are expected to reside in over-dense regions of the early universe, both due to their rarity and the requirement of continuous inflows of cold gas needed to grow their central SMBH to their observed sizes by $z \sim 6$. However, searches for associated galaxy over-densities around early quasars have yielded mixed results (e.g., Kim et al. 2009; Bañados et al. 2013; Champagne et al. 2018) with some quasar fields even appearing to be under-dense (Ota et al. 2018). A suggested cause for such under-densities is suppression of star formation by intense quasar radiation, which can prevent gas from cooling and delay the onset of star formation (Kashikawa et al. 2007) and even completely photoevaporate small haloes with $M_h \leqslant 1 \times 10^7 M_\odot$ on timescales of $\sim$100 Myr at 1 pMpc distance (Shapiro et al. 2004).

Since Aerith B is located $<$1 pMpc from J0836, and the quasar is brighter than those assumed by models in the literature, we wish to determine whether its star formation history could have been significantly impacted. UV intensity is traditionally measured with J_{21}, defined as

$$\frac{L(\lambda_{\text{LL}})}{16\pi^2 r^2} = J_{21}(r) \times 10^{-21} \text{ erg s}^{-1} \text{ cm}^{-2} \text{ Hz}^{-1} \text{ sr}^{-1}, \quad (15)$$

where $L(\lambda_{\text{LL}})$ is the quasar luminosity at the Lyman limit, and r is the distance to the quasar. We estimate $L(\lambda_{\text{LL}})$ based on the magnitude of the quasar in the y_{P1} and J magnitudes measured in Bañados et al. (2016), finding a continuum spectral hardness of $\beta = -1.4 \pm 0.1$ for a Lyman-limit luminosity of $L(\lambda_{\text{LL}}) = 3.0 \pm 0.4 \times 10^{32}$ erg s^{-1} Hz^{-1}. We obtain UV intensities of $J_{21} = 9.4^{+3.9}_{-2.9}$ at the location of Aerith C at the edge of the proximity zone, $J_{21} = 18^{+13}_{-5}$ for Aerith A, and $273 < J_{21} < 1970$ for Aerith B. The upper bound corresponds to the probably unphysical scenario where Aerith B is at the same redshift as the quasar, which is permitted within 1σ but would require a quasar opening angle of 90°.

In the model of Kashikawa et al. (2007), a UV intensity of $J_{21} \gtrsim 10$ implies that star formation should be suppressed entirely in haloes with $M_h < 3 \times 10^9 M_\odot$ in all of J0836's proximity zone. At the location of Aerith B, star formation is suppressed in dark matter haloes with $M_h < 10^{10} M_\odot$ and delayed by $\sim$30 Myr for haloes of mass $M_h < 3 \times 10^{10} M_\odot$. Chen (2019) predict a more stochastic suppression of star formation, resulting in a weaker effect overall than Kashikawa et al. (2007), although still qualitatively comparable.

Should star formation in the proximate LAEs have been delayed or even quenched by the quasar's proximity? Ouchi et al. (2018) estimated the mass of LAEs at $z \sim 5.7$ using an HOD model, and they found that LAEs with $L_{\text{Ly}\alpha} > L^*_{\text{Ly}\alpha} = 6.3 \times 10^{42}$ erg s^{-1} have an average host halo mass of $M = 1.2 \times 10^{11} M_\odot$ and a minimum mass of $M_{\text{min}} = 3.5 \times 10^9 M_\odot$. Aerith B and C are brighter than $L^*_{\text{Ly}\alpha}$ even discounting the extra emission in the blue peak of the Lyα line, implying that their star formation history would not be impacted if they reside in average-sized dark matter haloes. However, the lack of quenching implies a host halo mass of $M_h > 3 \times 10^{10} M_\odot$ for Aerith B, more stringent than the lower limit from the HOD model. Aerith A has a luminosity below $L^*_{\text{Ly}\alpha}$ (Table 2), but the lack of quenching still suggests a host halo mass larger than $\sim 10^{10} M_\odot$.

On average, one would expect a strong suppression of galaxies with $L_{\text{Ly}\alpha} < L^*_{\text{Ly}\alpha}$ inside J0836's proximity zone. This is tempered by variability both of the LAEs and the quasar. The degree of suppression of star formation in proximate galaxies depends on the status of star-forming processes at the time of quasar turn-on (cold gas reservoirs, ISM properties) as well as the duration of the current quasar phase and stochasticity (Chen 2019; Habouzit et al. 2019). Nevertheless, the field around J0836 is an ideal laboratory for testing quasar radiative suppression, as it will affect bright LAEs within current observational reach over a very large surface area of sky. Future analysis and observations will confirm whether the proximity zone is indeed over-dense in bright galaxies and under-dense in fainter ones, as predicted by models.

5.2. Implications for the Formation of $z \gtrsim 6$ SMBHs: Accretion Disks and the Host-galaxy Environment

The black hole mass of J0836 is very weakly constrained due to the lack of a clean Mg II emission line spectrum. However, as one of the brightest quasars at $z > 5.7$, a mass outside the range $(0.3 - 10) \times 10^9 M_\odot$ would be highly unexpected (Mazzucchelli et al. 2017; Bañados et al. 2018b). The growth of such SMBHs by $z \sim 6$ requires substantial gas accretion or massive seeds such as those produced by the direct collapse scenario or the collapse of dense star clusters (see, e.g., Haiman 2013; Inayoshi et al. 2019; Smith & Bromm 2019; Woods et al. 2019 for reviews). The *e*-folding accretion timescale for the black hole mass growth is (e.g., Madau et al. 2014)

$$t_{\rm acc}^{\rm BH} = 3.8 \times 10^8 \frac{\epsilon}{1-\epsilon}\left(\frac{L_{\rm bol}}{L_{\rm Edd}}\right)^{-1} \text{yr}. \quad (16)$$

For the conventional value of radiative efficiency, $\epsilon = 0.10$, assuming a thin accretion disk (Shakura & Sunyaev 1973), the timescale is $t_{\rm acc}^{\rm BH} = 4.2 \times 10^7$ yr at the Eddington limit.

An alternative estimate of the total quasar lifetime follows from the quasar clustering and luminosity function measurements, which constrain the population-averaged duty cycle $f_{\rm duty}$. The average total lifetime of quasar activity at $z = 5.8$ is then

$$\langle t_{\rm Q} \rangle \approx \frac{f_{\rm duty}\, t_{\rm H}(z = z_{\rm Q})}{1 - \cos\theta_{\rm Q}} \leqslant 1.12 \times 10^8 \text{ yr}\left(\frac{f_{\rm duty}}{0.1}\right), \quad (17)$$

using the bound of opening angle measured from the J0836 field. $f_{\rm duty}$ is uncertain by an order of magnitude, but 0.1 is a somewhat reasonable upper estimate (e.g., White et al. 2012, their Section 4.2; but see also Tanaka & Haiman 2009; Habouzit et al. 2017).

Our estimated age of the recent quasar activity of J0836 is clearly shorter than the *e*-folding timescale required to grow to an SMBH of $M_{\rm BH} \approx 2 \times 10^9\, M_\odot$ and much shorter that the total quasar lifetime. This implies transient, episodic super-Eddington gas accretion but with modest quasar activities to match the observed state of J0836, or sustained accretion in obscured phases.

Such fast intermittent gas accretion could be a consequence of *slim* accretion disks around high-redshift SMBHs (see Madau et al. 2014) where the radiation-dominated, advective flow of the disk naturally lowers the radiative efficiency ($\epsilon \sim 0.02$ & $L/L_{\rm Edd} \sim 1$) for super-Eddington accretion ($\dot{M}/\dot{M}_{\rm BH} > 1$), resulting in only mildly super-Eddington luminosity. The recent (general-relativistic) radiation magneto-hydrodynamic simulations of super-Eddington accretion disks (Jiang et al. 2014; McKinney et al. 2014; Sadowski & Narayan 2016) indicate that such a scenario arises as long as a vigorous inflow and a reservoir of gas around the disk is maintained. Observations of proximity zone morphologies of $z > 7$ provide evidence for radiative efficiencies $\epsilon < 0.1$ (Davies et al. 2019).

The megaparsec-scale over-density around J0836 indicated by the bright proximate LAEs supports that such a reservoir of gas around the quasar-host galaxy could be maintained, potentially triggering the occasional nuclear inflow by mergers or sustained cold accretion onto the galaxy. Frey et al. (2010) suggest that the compact observed radio size (~40 pc) of J0836 and its steep spectral index could result from interactions of a relativistic jet with the dense environment of the host galaxy, giving rise to emission peaked at frequencies of a few GHz (Falcke et al. 2004).

For comparison, $z \sim 3$ studies of transverse and line-of-sight He II proximity effects (Schmidt et al. 2017) and Lyα fluorescence sources around hyper-luminous quasars (Hennawi & Prochaska 2013; Trainor & Steidel 2013; Borisova et al. 2016) also indicate short durations of the radiative activity of quasars on $\sim 10^{6-7}$ yr timescales (see also Eilers et al. 2017, 2020; Davies et al. 2020). While many uncertainties remain, such findings seem to align with the above picture. Spectroscopic follow up of quasar fields, piloted with J0836, shows a clear way forward demonstrating the capability of proximate LAEs as a laboratory to constrain the formation and growth of the first SMBHs.

5.3. Possible Effect of Lyα Fluorescence

The Lyα luminosities of the proximate LAEs could include a contribution from Lyα fluorescence caused by the quasar's ionization field, in addition to star formation (e.g., Cantalupo et al. 2005; Hennawi & Prochaska 2013). The amount of Lyα fluorescence imparted on a system with H I column density $N_{\rm H\,I}$ and cross section $\sigma_{\rm LAE}$ at a distance r away from the quasar is given by

$$L_\alpha^{\rm fl.} = \frac{2}{3} h\nu_\alpha f_\phi \int_{\nu_{\rm L}}^{\infty} (1 - e^{-\sigma_\nu N_{\rm HI}}) \frac{\sigma_{\rm LAE}}{4\pi r^2} \frac{L_\nu^{\rm QSO}}{h\nu} d\nu,$$
$$\simeq \frac{2}{3} h\nu_\alpha f_\phi \frac{\sigma_{\rm LAE}}{4\pi r^2} \dot{N}_{\rm ion}^{\rm QSO}, \text{ for } N_{\rm HI} \gg 10^{17}\ \text{cm}^{-2}, \quad (18)$$

where f_ϕ is the illumination fraction.[8] Assuming the geometrical cross section $\sigma_{\rm LAE} = \pi r_{\rm size}^2$ with radius $r_{\rm size}$, the fluorescent Lyα luminosity in our objects is

$$L_\alpha^{\rm fl.} \approx 2.7 \times 10^{41} r_{\rm Mpc}^{-2} \left(\frac{r_{\rm size}}{5\text{ kpc}}\right)^2 \left(\frac{\dot{N}_{\rm ion}^{\rm QSO}}{4 \times 10^{57}\ \text{s}^{-1}}\right) \text{erg s}^{-1}. \quad (19)$$

The size of an LAE is typically $\lesssim$2 pkpc (Shibuya et al. 2019); we adopt a value of 5pkpc as an upper estimate.

The above calculation indicates that Lyα fluorescence accounts for <1% of the observed Lyα luminosity for Aerith A and C. Up to 22% of L_α could originate from fluorescence in Aerith B, but this would occur in the unrealistic scenario of a $\theta = 90°$ opening angle. Conservative bounds for the fluorescence contribution are [2%, 22%]. The Lyα luminosities of the objects are in close agreement with the expected values based on their UV luminosities and star formation rates, suggesting that any fluorescent Lyα contribution due to J0836's ionizing field is likely minor.

5.4. Future Prospects

While the serendipitous discovery of our proximate LAEs was unquestionably aided by the extreme luminosity of J0836, there is no reason why such objects could not be found at

[8] For a spherical cloud, the illumination fraction is $f_\phi = 1 - \phi/\pi$ where ϕ is the phase angle between the quasar-cloud-observer, having $f_\phi = 0$, $\phi = \pi$ if all fluorescent Lyα is backscattered away from us, $f_\phi = 0.5$ for half-moon ($\phi = \pi/2$) illumination, and $\phi = 0$ if the fluorescent Lyα is scattered out into the line of sight. For a cloud consisting of tiny cloudlet structures, the fluorescent Lyα can be scattered within the cloud and redirected to us. Thus, the value of f_ϕ can become larger than a solid spherical geometry. Here, we assume the conservative upper bound contribution of $f_\phi = 1$.

smaller separations from fainter quasars. Over 30 (and growing) fields around $z > 5.7$ quasars have been observed with integral field spectroscopy by the MUSE instrument (Farina et al. 2019). Finding additional proximate LAEs offers a clear path to refining the results presented in this paper.

With a larger sample, proximate LAEs will constrain models of reionization. Faint galaxies are expected to provide the majority of reionization photons, but scenarios driven by bright galaxies are still permitted (Meyer et al. 2019c). In the model of Naidu et al. (2020), galaxies brighter than $M_{\rm UV} = -20$ can power reionization alone if their escapes fractions are $f_{\rm esc} \geqslant 0.20$. Proximate LAEs provide the most direct way of measuring $f_{\rm esc}$ in individual bright and faint galaxies, and they will eventually rule in favor or against existing predictions. In addition, numerical models are resolving the physical properties of galaxies in the first billion years in increasingly fine detail (e.g., Pallottini et al. 2017). It will be interesting to see if those frameworks can account for LyC leakage from some bright galaxies during the EoR, but not others.

Some model of the neutral IGM's effect on LAEs predict that the red peak of Lyα, in addition to the blue peak, will be suppressed on average by a damping wing of neutral hydrogen absorption (e.g., Dijkstra et al. 2007). It is interesting to note that our three galaxies, although presumably less affected by this than the general $z \sim 5.8$ LAE population, are slightly faint in Lyα for their $M_{\rm UV}$ (Figure 6). In the future, larger samples of proximate LAEs may make it possible to reconstruct an "intrinsic" Lyα luminosity distribution function and disentangle changes in the IGM and the CMG of early galaxies. At $z > 6$, this may offer a path to measuring the IGM damping wing in a statistical sense.

6. Summary

We have discovered the first three proximate LAEs in the proximity zone of quasar J0836+0054 at $z = 5.795$. The intense ionizing radiation in their surroundings reveals unique properties never observed before at $z > 5$. To understand these observations in the context of the central quasar, we have modeled the ionization and density structure of the proximity zone and put constraints on the central quasar's properties. Our main findings are as follows:

1. Aerith B displays the first widely separated Lyα emission line seen in a galaxy during reionization. Unlike previously detected Lyα double peaks at $z > 6.5$, the morphology and luminosity of Aerith B's Lyα line is normal and even typical compared to $2 < z < 3$ LAEs.
2. The morphology of the Lyα line in Aerith B implies an escape fraction of ionizing radiation $f_{\rm esc} \simeq 0.01$ based on the double-peak separation/LyC leakage correlation, which is well calibrated at low z. This implies that not all bright galaxies ($M_{\rm UV} = -21$) during the EoR are strong leakers, in tension with some models of reionization.
3. Fitting the Lyα line morphology with an outflowing shell model, we find best-fit ISM properties of Aerith B implying a typical central $N_{\rm H}$ density, gas outflow speed, and dust opacity compared to the $2 < z < 3$ LAE population.
4. The star formation in Aerith B has not been quenched, despite being exposed to an ionizing intensity of $J_{21} > 273$. This might imply it is hosted in a dark matter halo with mass $M_h > 3 \times 10^{10} M_{\odot}$ or that it assembled its stellar mass before quasar turn-on.
5. Aerith A is detected at 10σ in a narrowband filter at a wavelength shorter than Lyα. The covered wavelength range significantly overlaps with J0836's proximity zone, making this the first detection of the Lyα transverse proximity effect. Modeling the propagation of ionizing photons around J0836, we find the level of transmission toward Aerith A ($\tau_{\rm NB} = 1.2^{+0.4}_{-0.3}$) to be entirely consistent with the quasar's UV magnitude assuming a far-UV slope of $\beta = -1.4$. The ionizing emission of J0836 is therefore not significantly obscured.
6. J0836's current quasar phase started 2.1×10^5 yr $< t_{\rm age} < 2.8 \times 10^7$ yr ago, based on the lack of continuum transmission immediately bluewards of Aerith A's Lyα line (2.4σ). This is the first measurement of its kind and is consistent with theoretical expectations from the literature.
7. Aerith C displays an emission line that lines up closely ($\Delta z = 0.02$) with the formal end of J0836's proximity zone. The following distance at which transmission falls below 10% is $r = 13$ pMpc, in close agreement expectations from our model based on J0836's UV magnitude. Such an extended proximity zone would be the largest ever detected around an EoR quasar.
8. The UV continuum in Aerith C appears to be offset from the location of the detected emission line by 6.3 pkpc. Such an offset is larger than previously observed at high z, suggesting a larger over-density of galaxies.

S.B., K.K., R.M., and N.L. acknowledge funding from the European Research Council (ERC) under the European Union's Horizon 2020 research and innovation program (grant agreement No. 669253). M.G. was supported by NASA through the NASA Hubble Fellowship grant HST-HF2-51409. Based in part on data collected at Subaru Telescope, which is operated by the National Astronomical Observatory of Japan. Some of the data presented herein were obtained at the W. M. Keck Observatory, which is operated as a scientific partnership among the California Institute of Technology, the University of California, and the National Aeronautics and Space Administration. The Observatory was made possible by the generous financial support of the W. M. Keck Foundation.

The authors recognize and acknowledge the very significant cultural role and reverence that the summit of Maunakea has always had within the indigenous Hawaiian community. We are most fortunate to have the opportunity to conduct observations from this mountain.

Facility: Keck:II (DEIMOS).

ORCID iDs

Sarah E. I. Bosman https://orcid.org/0000-0001-8582-7012
Koki Kakiichi https://orcid.org/0000-0001-6874-1321
Romain A. Meyer https://orcid.org/0000-0001-5492-4522
Max Gronke https://orcid.org/0000-0003-2491-060X
Nicolas Laporte https://orcid.org/0000-0001-7459-6335
Richard S. Ellis https://orcid.org/0000-0001-7782-7071

References

Adams, T. F. 1972, ApJ, 174, 439
Adelberger, K. L. 2004, ApJ, 612, 706
Ahn, S.-H., Lee, H.-W., & Lee, H. M. 2003, MNRAS, 340, 863

Ajiki, M., Taniguchi, Y., Murayama, T., et al. 2006, PASJ, 58, 499
Bañados, E., Carilli, C., Walter, F., et al. 2018a, ApJL, 861, L14
Bañados, E., Venemans, B., Walter, F., et al. 2013, ApJ, 773, 178
Bañados, E., Venemans, B. P., Decarli, R., et al. 2016, ApJS, 227, 11
Bañados, E., Venemans, B. P., Mazzucchelli, C., et al. 2018b, Natur, 553, 473
Bañados, E., Venemans, B. P., Morganson, E., et al. 2015, ApJ, 804, 118
Becker, G. D., Bolton, J. S., & Lidz, A. 2015a, PASA, 32, e045
Becker, G. D., Bolton, J. S., Madau, P., et al. 2015b, MNRAS, 447, 3402
Becker, G. D., Davies, F. B., Furlanetto, S. R., et al. 2018, ApJ, 863, 92
Becker, G. D., Rauch, M., & Sargent, W. L. W. 2007, ApJ, 662, 72
Bertin, E., & Arnouts, S. 1996, A&AS, 117, 393
Blanton, M. R., Bershady, M. A., Abolfathi, B., et al. 2017, AJ, 154, 28
Bolton, J. S., & Haehnelt, M. G. 2007, MNRAS, 382, 325
Bolton, J. S., & Haehnelt, M. G. 2013, MNRAS, 429, 1695
Bolton, J. S., Haehnelt, M. G., Warren, S. J., et al. 2011, MNRAS, 416, L70
Bonilha, J. R. M., Ferch, R., Salpeter, E. E., Slater, G., & Noerdlinger, P. D. 1979, ApJ, 233, 649
Borisova, E., Lilly, S. J., Cantalupo, S., et al. 2016, ApJ, 830, 120
Bosman, S. 2020, All $z > 5.7$ quasars currently known, v1.4., Zenodo, doi:10.5281/zenodo.3634964
Bosman, S. E. I., Becker, G. D., Haehnelt, M. G., et al. 2017, MNRAS, 470, 1919
Bosman, S. E. I., Fan, X., Jiang, L., et al. 2018, MNRAS, 479, 1055
Cantalupo, S., Porciani, C., Lilly, S. J., & Miniati, F. 2005, ApJ, 628, 61
Carilli, C. L., Wang, R., Fan, X., et al. 2010, ApJ, 714, 834
Carniani, S., Maiolino, R., Amorin, R., et al. 2018, MNRAS, 478, 1170
Carniani, S., Maiolino, R., Pallottini, A., et al. 2017, A&A, 605, A42
Carswell, R. F., & Webb, J. K. 2014, VPFIT: Voigt Profile Fitting Program, v10.4, Astrophysics Source Code Library, ascl:1408.015
Cassata, P., Morselli, L., Faisst, A., et al. 2020, arXiv:2002.00967
Cen, R., & Kimm, T. 2015, ApJL, 801, L25
Chabrier, G. 2003, PASP, 115, 763
Champagne, J. B., Decarli, R., Casey, C. M., et al. 2018, ApJ, 867, 153
Chardin, J., Haehnelt, M. G., Aubert, D., & Puchwein, E. 2015, MNRAS, 453, 2943
Chen, H. 2019, arXiv:1911.09113
Choudhury, T. R., Puchwein, E., Haehnelt, M. G., & Bolton, J. S. 2015, MNRAS, 452, 261
Concas, A., & Popesso, P. 2019, MNRAS, 486, L91
Conroy, C., & White, M. 2013, ApJ, 762, 70
Cooper, M. C., Newman, J. A., Davis, M., Finkbeiner, D. P., & Gerke, B. F. 2012, spec2d: DEEP2 DEIMOS Spectral Pipeline, v1.1.4, Astrophysics Source Code Library, ascl:1203.003
Cooper, T. J., Simcoe, R. A., Cooksey, K. L., et al. 2019, ApJ, 882, 77
Davies, F. B. 2020, MNRAS, 494, 2937
Davies, F. B., & Furlanetto, S. R. 2016, MNRAS, 460, 1328
Davies, F. B., Hennawi, J. F., & Eilers, A.-C. 2019, ApJL, 884, L19
Davies, F. B., Hennawi, J. F., & Eilers, A.-C. 2020, MNRAS, 493, 1330
Decarli, R., Walter, F., Venemans, B. P., et al. 2018, ApJ, 854, 97
Dijkstra, M., Gronke, M., & Venkatesan, A. 2016, ApJ, 828, 71
Dijkstra, M., Lidz, A., & Wyithe, J. S. B. 2007, MNRAS, 377, 1175
Ding, J., Cai, Z., Fan, X., et al. 2017, ApJL, 838, L22
Durovčíková, D., Katz, H., Bosman, S. E. I., et al. 2020, MNRAS, 493, 4256
Eilers, A.-C., Davies, F. B., Hennawi, J. F., et al. 2017, ApJ, 840, 24
Eilers, A.-C., Davies, F. B., & Hennawi, J. F. 2018, ApJ, 864, 53
Eilers, A.-C., Hennawi, J. F., Decarli, R., et al. 2020, arXiv:2002.01811
Erb, D. K., Steidel, C. C., Trainor, R. F., et al. 2014, ApJ, 795, 33
Faber, S. M., Phillips, A. C., Kibrick, R. I., et al. 2003, Proc. SPIE, 4841, 1657
Falcke, H., Körding, E., & Markoff, S. 2004, A&A, 414, 895
Fan, X., Narayanan, V. K., Lupton, R. H., et al. 2001, AJ, 122, 2833
Fan, X., Strauss, M. A., Becker, R. H., et al. 2006, AJ, 132, 117
Farina, E. P., Arrigoni-Battaia, F., Costa, T., et al. 2019, ApJ, 887, 196
Faucher-Giguère, C.-A., Lidz, A., Hernquist, L., & Zaldarriaga, M. 2008, ApJL, 682, L9
Fletcher, T. J., Tang, M., Robertson, B. E., et al. 2019, ApJ, 878, 87
Frey, S., Paragi, Z., Gurvits, L. I., Cseh, D., & Gabányi, K. É 2010, A&A, 524, A83
Frey, S., Paragi, Z., Mosoni, L., & Gurvits, L. I. 2005, A&A, 436, L13
Fumagalli, M., O'Meara, J. M., & Prochaska, J. X. 2016, MNRAS, 455, 4100
Furlanetto, S. R., Zaldarriaga, M., & Hernquist, L. 2006, MNRAS, 365, 1012
Greig, B., Mesinger, A., Haiman, Z., & Simcoe, R. A. 2017, MNRAS, 466, 4239
Gronke, M. 2017, A&A, 608, A139
Gronke, M., Bull, P., & Dijkstra, M. 2015, ApJ, 812, 123
Gronke, M., Dijkstra, M., McCourt, M., & Peng, Oh, S. 2017, A&A, 607, A71
Habouzit, M., Volonteri, M., & Dubois, Y. 2017, MNRAS, 468, 3935
Habouzit, M., Volonteri, M., Somerville, R. S., et al. 2019, MNRAS, 489, 1206
Haiman, Z. 2013, in The First Galaxies, ed. T. Wiklind, B. Mobasher, & V. Bromm (Berlin: Springer), 293
Haiman, Z., & Cen, R. 2001, in ASP Conf. Ser. 222, The Physics of Galaxy Formation, ed. M. Umemura & H. Susa (San Francisco, CA: ASP), 101
Harikane, Y., Ouchi, M., Ono, Y., et al. 2019, arXiv:1902.09555
Hashimoto, T., Verhamme, A., Ouchi, M., et al. 2015, ApJ, 812, 157
Hayes, M. 2015, PASA, 32, e027
Hennawi, J. F., & Prochaska, J. X. 2013, ApJ, 766, 58
Hennawi, J. F., Prochaska, J. X., Burles, S., et al. 2006, ApJ, 651, 61
Higuchi, R., Ouchi, M., Ono, Y., et al. 2019, ApJ, 879, 28
Hopkins, P. F., Torrey, P., Faucher-Giguère, C.-A., Quataert, E., & Murray, N. 2016, MNRAS, 458, 816
Hu, E. M., Cowie, L. L., Barger, A. J., et al. 2010, ApJ, 725, 394
Hu, E. M., Cowie, L. L., Songaila, A., et al. 2016, ApJL, 825, L7
Inayoshi, K., Visbal, E., & Haiman, Z. 2019, arXiv:1911.05791
Izotov, Y. I., Orlitová, I., Schaerer, D., et al. 2016a, Natur, 529, 178
Izotov, Y. I., Schaerer, D., Thuan, T. X., et al. 2016b, MNRAS, 461, 3683
Izotov, Y. I., Worseck, G., Schaerer, D., et al. 2018, MNRAS, 478, 4851
Jaskot, A. E., & Oey, M. S. 2013, ApJ, 766, 91
Jiang, L., Egami, E., Fan, X., et al. 2013, ApJ, 773, 153
Jiang, L., Wu, J., Bian, F., et al. 2018, NatAs, 2, 962
Jiang, Y.-F., Stone, J. M., & Davis, S. W. 2014, ApJ, 796, 106
Kaifu, N., Usuda, T., Hayashi, S. S., et al. 2000, PASJ, 52, 1
Kakiichi, K., & Dijkstra, M. 2018, MNRAS, 480, 5140
Kakiichi, K., Dijkstra, M., Ciardi, B., & Graziani, L. 2016, MNRAS, 463, 4019
Kakiichi, K., Ellis, R. S., Laporte, N., et al. 2018, MNRAS, 479, 43
Kakiichi, K., & Gronke, M. 2019, arXiv:1905.02480
Karman, W., Caputi, K. I., Caminha, G. B., et al. 2017, A&A, 599, A28
Kashikawa, N., Kitayama, T., Doi, M., et al. 2007, ApJ, 663, 765
Kashino, D., Lilly, S. J., Shibuya, T., Ouchi, M., & Kashikawa, N. 2020, ApJ, 888, 6
Katz, H., Galligan, T. P., Kimm, T., et al. 2019, MNRAS, 487, 5902
Keating, L. C., Puchwein, E., Haehnelt, M. G., Bird, S., & Bolton, J. S. 2016, MNRAS, 461, 606
Kelly, B. C., Bechtold, J., & Siemiginowska, A. 2009, ApJ, 698, 895
Kelly, B. C., Becker, A. C., Sobolewska, M., Siemiginowska, A., & Uttley, P. 2014, ApJ, 788, 33
Kennicutt, Robert C. J. 1998, ARA&A, 36, 189
Kim, S., Stiavelli, M., Trenti, M., et al. 2009, ApJ, 695, 809
Kimm, T., Blaizot, J., Garel, T., et al. 2019, MNRAS, 486, 2215
Konno, A., Ouchi, M., Shibuya, T., et al. 2018, PASJ, 70, S16
Kulas, K. R., Shapley, A. E., Kollmeier, J. A., et al. 2012, ApJ, 745, 33
Kulkarni, G., Keating, L. C., Haehnelt, M. G., et al. 2019, MNRAS, 485, L24
Kurk, J. D., Walter, F., Fan, X., et al. 2007, ApJ, 669, 32
Laursen, P., Sommer-Larsen, J., & Razoumov, A. O. 2011, ApJ, 728, 52
Lidz, A., Hopkins, P. F., Cox, T. J., Hernquist, L., & Robertson, B. 2006, ApJ, 641, 41
Madau, P., Haardt, F., & Dotti, M. 2014, ApJL, 784, L38
Madau, P., & Rees, M. J. 2000, ApJL, 542, L69
Maiolino, R., Carniani, S., Fontana, A., et al. 2015, MNRAS, 452, 54
Maiolino, R., Neri, R., Beelen, A., et al. 2007, A&A, 472, L33
Mallery, R. P., Mobasher, B., Capak, P., et al. 2012, ApJ, 760, 128
Marchi, F., Pentericci, L., Guaita, L., et al. 2018, A&A, 614, A11
Mason, C. A., Treu, T., Dijkstra, M., et al. 2018, ApJ, 856, 2
Matthee, J., Sobral, D., Darvish, B., et al. 2017, MNRAS, 472, 772
Matthee, J., Sobral, D., Gronke, M., et al. 2018, A&A, 619, A136
Matthee, J., Sobral, D., Santos, S., et al. 2015, MNRAS, 451, 400
Mazzucchelli, C., Bañados, E., Venemans, B. P., et al. 2017, ApJ, 849, 91
McGreer, I. D., Mesinger, A., & D'Odorico, V. 2015, MNRAS, 447, 499
McKinney, J. C., Tchekhovskoy, A., Sadowski, A., & Narayan, R. 2014, MNRAS, 441, 3177
McQuinn, M., Hernquist, L., Zaldarriaga, M., & Dutta, S. 2007, MNRAS, 381, 75
Mesinger, A., Aykutalp, A., Vanzella, E., et al. 2015, MNRAS, 446, 566
Meyer, R. A., Bosman, S. E. I., & Ellis, R. S. 2019a, MNRAS, 487, 3305
Meyer, R. A., Bosman, S. E. I., Kakiichi, K., & Ellis, R. S. 2019b, MNRAS, 483, 19
Meyer, R. A., Kakiichi, K., Bosman, S. E. I., et al. 2019c, arXiv:1912.04314
Miyazaki, S., Komiyama, Y., Sekiguchi, M., et al. 2002, PASJ, 54, 833
Naidu, R. P., Tacchella, S., Mason, C. A., et al. 2020, ApJ, 892, 109
Neufeld, D. A. 1990, ApJ, 350, 216
Newman, J. A., Cooper, M. C., Davis, M., et al. 2013, ApJS, 208, 5
Novak, G. S., Ostriker, J. P., & Ciotti, L. 2011, ApJ, 737, 26
Oke, J. B., & Gunn, J. E. 1983, ApJ, 266, 713

Orlitová, I., Verhamme, A., Henry, A., et al. 2018, A&A, 616, A60
Ota, K., Venemans, B. P., Taniguchi, Y., et al. 2018, ApJ, 856, 109
Ouchi, M., Harikane, Y., Shibuya, T., et al. 2018, PASJ, 70, S13
Ouchi, M., Shimasaku, K., Akiyama, M., et al. 2008, ApJS, 176, 301
Ouchi, M., Shimasaku, K., Furusawa, H., et al. 2010, ApJ, 723, 869
Ouchi, M., Shimasaku, K., Okamura, S., et al. 2004, ApJ, 611, 660
Overzier, R. A., Guo, Q., Kauffmann, G., et al. 2009, MNRAS, 394, 577
Pallottini, A., Ferrara, A., Bovino, S., et al. 2017, MNRAS, 471, 4128
Paulino-Afonso, A., Sobral, D., Darvish, B., et al. 2018, A&A, 620, A186
Pawlik, A. H., Schaye, J., & van Scherpenzeel, E. 2009, MNRAS, 394, 1812
Pentericci, L., Vanzella, E., Fontana, A., et al. 2014, ApJ, 793, 113
Planck Collaboration, Adam, R., Aghanim, N., et al. 2016, A&A, 596, A108
Prochaska, J. X., Hennawi, J., Cooke, R., et al. 2019, pypeit/PypeIt: Releasing for DOI, v11.0.1, Zenodo, doi:10.5281/zenodo.3506873
Prochaska, J. X., Worseck, G., & O'Meara, J. M. 2009, ApJL, 705, L113
Pushkarev, A. B., Kovalev, Y. Y., Lister, M. L., & Savolainen, T. 2017, MNRAS, 468, 4992
Rivera-Thorsen, T. E., Hayes, M., Östlin, G., et al. 2015, ApJ, 805, 14
Robertson, B. E., Ellis, R. S., Furlanetto, S. R., & Dunlop, J. S. 2015, ApJL, 802, L19
Robertson, B. E., Furlanetto, S. R., Schneider, E., et al. 2013, ApJ, 768, 71
Rudie, G. C., Steidel, C. C., Trainor, R. F., et al. 2012, ApJ, 750, 67
Sadowski, A., & Narayan, R. 2016, MNRAS, 456, 3929
Salpeter, E. E. 1955, ApJ, 121, 161
Santos, S., Sobral, D., & Matthee, J. 2016, MNRAS, 463, 1678
Sartori, L. F., Schawinski, K., Trakhtenbrot, B., et al. 2018, MNRAS, 476, L34
Schmidt, T. M., Hennawi, J. F., Lee, K.-G., et al. 2019, ApJ, 882, 165
Schmidt, T. M., Worseck, G., Hennawi, J. F., Prochaska, J. X., & Crighton, N. H. M. 2017, ApJ, 847, 81
Shakura, N. I., & Sunyaev, R. A. 1973, A&A, 500, 33
Shapiro, P. R., Iliev, I. T., & Raga, A. C. 2004, MNRAS, 348, 753
Shen, Y., Strauss, M. A., Oguri, M., et al. 2007, AJ, 133, 2222
Shen, Y., Wu, J., Jiang, L., et al. 2019, ApJ, 873, 35
Shibuya, T., Ouchi, M., Harikane, Y., et al. 2018, PASJ, 70, S15
Shibuya, T., Ouchi, M., Harikane, Y., & Nakajima, K. 2019, ApJ, 871, 164
Smith, A., & Bromm, V. 2019, ConPh, 60, 111
Sobral, D., & Matthee, J. 2019, A&A, 623, A157
Sobral, D., Santos, S., Matthee, J., et al. 2018, MNRAS, 476, 4725
Songaila, A., Hu, E. M., Barger, A. J., et al. 2018, ApJ, 859, 91
Stark, D. P. 2016, ARA&A, 54, 761
Stark, D. P., Ellis, R. S., Chiu, K., Ouchi, M., & Bunker, A. 2010, MNRAS, 408, 1628
Steidel, C. C., Erb, D. K., Shapley, A. E., et al. 2010, ApJ, 717, 289
Stern, D., Hall, P. B., Barrientos, L. F., et al. 2003, ApJL, 596, L39
Tanaka, T., & Haiman, Z. 2009, ApJ, 696, 1798
Telfer, R. C., Zheng, W., Kriss, G. A., & Davidsen, A. F. 2002, ApJ, 565, 773
Trainor, R., & Steidel, C. C. 2013, ApJL, 775, L3
Trainor, R. F., Steidel, C. C., Strom, A. L., & Rudie, G. C. 2015, ApJ, 809, 89
Uhlenbeck, G. E., & Ornstein, L. S. 1930, PhRv, 36, 823
Vanzella, E., De Barros, S., Cupani, G., et al. 2016, ApJL, 821, L27
Vanzella, E., Nonino, M., Cupani, G., et al. 2018, MNRAS, 476, L15
Venemans, B. P., Walter, F., Zschaechner, L., et al. 2016, ApJ, 816, 37
Verhamme, A., Orlitová, I., Schaerer, D., et al. 2017, A&A, 597, A13
Verhamme, A., Orlitová, I., Schaerer, D., & Hayes, M. 2015, A&A, 578, A7
Verhamme, A., Schaerer, D., Atek, H., & Tapken, C. 2008, A&A, 491, 89
Vernet, J., Dekker, H., D'Odorico, S., et al. 2011, A&A, 536, A105
Visbal, E., & Croft, R. A. C. 2008, ApJ, 674, 660
Vogt, S. S., Allen, S. L., Bigelow, B. C., et al. 1994, Proc. SPIE., 2198, 362
Walter, F., Riechers, D., Cox, P., et al. 2009, Natur, 457, 699
Wang, R., Carilli, C. L., Beelen, A., et al. 2007, AJ, 134, 617
Weinberger, L. H., Kulkarni, G., Haehnelt, M. G., Choudhury, T. R., & Puchwein, E. 2018, MNRAS, 479, 2564
White, M., Myers, A. D., Ross, N. P., et al. 2012, MNRAS, 424, 933
Woods, T. E., Agarwal, B., Bromm, V., et al. 2019, PASA, 36, e027
Worseck, G., Prochaska, J. X., O'Meara, J. M., et al. 2014, MNRAS, 445, 1745
Wyithe, J. S. B., Loeb, A., & Carilli, C. 2005, ApJ, 628, 575
Yagi, M., Kashikawa, N., Sekiguchi, M., et al. 2002, AJ, 123, 66
Yamada, T., Matsuda, Y., Kousai, K., et al. 2012, ApJ, 751, 29
Yang, H., Malhotra, S., Gronke, M., et al. 2017, ApJ, 844, 171
Zheng, W., Overzier, R. A., Bouwens, R. J., et al. 2006, ApJ, 640, 574
Zheng, Z.-Y., Wang, J., Rhoads, J., et al. 2017, ApJL, 842, L22